WIND RETRIEVAL ALGORITHMS FOR THE IWRAP AND HIWRAP AIRBORNE DOPPLER RADARS WITH APPLICATIONS TO HURRICANES

Stephen R. Guimond[1, 2], Lin Tian[2, 3], Gerald M. Heymsfield[2] and Stephen J. Frasier[4]

[1]*University of Maryland/Earth System Science Interdisciplinary Center (ESSIC)*
[2]*NASA Goddard Space Flight Center*
[3]*Morgan State University/GESTAR*
[4]*Microwave Remote Sensing Laboratory, University of Massachusetts*

Submitted to the *Journal of Atmospheric and Oceanic Technology*

June 25, 2013

Corresponding author address: Stephen R. Guimond, NASA Goddard Space Flight Center, Code 612, Greenbelt, MD 20771.
E-mail: stephen.guimond@nasa.gov

ABSTRACT

Algorithms for the retrieval of atmospheric winds in precipitating systems from downward-pointing, conically-scanning airborne Doppler radars are presented. The focus in the paper is on two radars: the Imaging Wind and Rain Airborne Profiler (IWRAP) and the High-altitude IWRAP (HIWRAP). The IWRAP is a dual-frequency (C and Ku band), multi-beam (incidence angles of 30° – 50°) system that flies on the NOAA WP-3D aircraft at altitudes of 2 – 4 km. The HIWRAP is a dual-frequency (Ku and Ka band), dual-beam (incidence angles of 30° and 40°) system that flies on the NASA Global Hawk aircraft at altitudes of 18 – 20 km.

Retrievals of the three Cartesian wind components over the entire radar sampling volume are described, which can be determined using either a traditional least squares or variational solution procedure. The random errors in the retrievals are evaluated using both an error propagation analysis and a numerical simulation of a hurricane. These analyses show that the vertical and along-track wind errors have strong across-track dependence with values of 0.25 m s^{-1} at nadir to 2.0 m s^{-1} and 1.0 m s^{-1} at the swath edges, respectively. The across-track wind errors also have across-track structure and are on average, 3.0 – 3.5 m s^{-1} or 10% of the hurricane wind speed. For typical rotated figure four flight patterns through hurricanes, the zonal and meridional wind speed errors are 2 – 3 m s^{-1}.

Examples of measured data retrievals from IWRAP during an eyewall replacement cycle in Hurricane Isabel (2003) and from HIWRAP during the development of Tropical Storm Matthew (2010) are shown.

1. Introduction

Knowledge of the three-dimensional distribution of winds in precipitating storm systems is crucial for understanding their dynamics and predicting their evolution. The horizontal components of the wind contain the vast majority of the kinetic energy integrated over these systems and are responsible for structural damage to buildings and homes as well as providing energy input to the ocean. The vertical component of the wind is the heart of the precipitating storm system, playing a key role in the formation of precipitation and the release of latent heat, which drives the dynamics. For those systems that spend the majority of their lifetime over ocean, such as tropical cyclones (TCs; our focus in this paper), airborne Doppler radar is the primary tool used to measure and calculate the three-dimensional winds.

There are several different airborne Doppler radar platforms used for TC research and operations. The X-band Tail (TA) Doppler radar on the NOAA WP-3D aircraft scans in a plane perpendicular to the aircraft with the antenna typically alternating fore/aft yielding along-track sampling of ~ 1.50 km with 0.15 km gate spacing (Gamache et al. 1995). Another X-band radar system operated by NCAR called ELDORA has a similar scanning geometry to the NOAA radar with the exception of a faster antenna rotation rate providing along-track sampling of ~ 0.40 km with 0.15 km gate spacing (Hildebrand et al. 1996). A NASA X-band radar system that flies on the ER-2 aircraft called EDOP has two fixed antennae, one pointing 33° forward and the other pointing at nadir, providing ~ 0.10 km along-track sampling and 0.04 km gate spacing (Heymsfield et al. 1996).

Doppler radars only measure the velocity of precipitation particles in the along-beam (radial relative to the radar) direction and thus, retrieval algorithms are necessary to compute the three-dimensional winds. There are several methods for retrieving wind fields from airborne Doppler radars. One of the earliest techniques used was to fly two radar-equipped aircraft with orthogonal legs, which allows calculation of the horizontal wind components by interpolating the radial velocities to common grid points and solving the Doppler velocity projection equations (e.g. Marks and Houze 1984). Using methods of this type, the vertical wind can be estimated by using the computed horizontal winds to integrate the anelastic mass continuity equation in the vertical with appropriate boundary conditions (e.g. Bohne and Srivastava 1975; Ray et al. 1980; Marks et al. 1992).

A more modern technique for computing the three components of the wind from scanning airborne Doppler radars (NOAA TA and ELDORA) involves solving an optimization problem by minimizing a cost function that contains terms describing the misfit between modeled and observed radial velocities and possibly dynamical constraints on the wind field (e.g. Ziegler 1978; Chong and Campos 1996; Gao et al. 1999; Reasor et al. 2009; Lopez-Carrillo and Raymond 2011; Bell et al. 2012). There are two main advantages of using this technique over the older methods described above: (1) improved accuracy of the vertical wind component by eliminating the explicit integration of the anelastic mass continuity equation (Gao et al. 1999) and (2) improved accuracy of the horizontal and vertical wind components by reducing the time delay between radar views of the same grid cell (relative to flying two orthogonal legs). Even though the accuracy of the vertical wind has been improved using this method, significant errors are still possible (Matejka and Bartels 1998).

Lastly, a method for computing two components of the wind from scanning airborne radars in the nadir (and/or zenith) plane is to combine only the antenna positions forward and aft of the aircraft, which yields exact expressions for the vertical and along-track velocity. This is a unique situation of the COPLAN method (Armijo 1969; Lhermitte 1970) utilized by the NASA EDOP radar. As with every wind retrieval technique, there are positive and negative attributes of this method. The main advantages are: (1) highly accurate vertical and along-track winds due to the ability to form exact expressions for these components and (2) higher horizontal resolution grids (grid spacing typically equal to the along-track sampling) compared to other methods because only two radar views are necessary to compute the winds. The drawbacks of this method are the inability to retrieve all three Cartesian wind components, as retrievals are only possible in a two-dimensional plane along the aircraft track. In addition, for flight tracks not aligned along a Cardinal direction or radial from a TC center, the interpretation of the along-track wind component for hurricane dynamics research is complicated.

The purpose of this paper is to describe wind retrieval algorithms that have been developed for a relatively new class of remote sensing instrument for TC studies: the downward pointing, conically scanning airborne Doppler radar. One of these radars, the Imaging Wind and Rain Airborne Profiler (IWRAP) has been operating on the NOAA WP-3D aircraft since 2002 collecting data from storm systems in a wide variety of intensity stages (e.g. Fernandez et al. 2005). The other radar, the High-altitude Imaging Wind and Rain Airborne Profiler (HIWRAP), is new and flew on the Global Hawk (GH) unmanned aircraft for the first time in 2010 during a NASA hurricane field experiment called GRIP (Genesis and Rapid Intensification Processes; Braun et al. 2013). An additional motivation for this paper is to briefly illustrate the TC science capabilities of both IWRAP and HIWRAP. The novelty of this study is in the application and understanding of the wind retrieval algorithms to the IWRAP/HIWRAP class of airborne radars as well as the detailed uncertainty analysis.

The paper is organized as follows: Section 2 introduces IWRAP and HIWRAP and presents wind retrieval algorithms tailored to the unique scanning geometry of these radars. In addition, an error propagation analysis with least squares theory is derived for one of these retrieval algorithms. Section 3 presents the error characteristics of the wind retrieval algorithms using a realistic numerical simulation of a hurricane. Section 4 shows examples of IWRAP and HIWRAP wind retrievals from measured TC data. Finally, a summary of the paper and conclusions are presented in section 5.

2. Wind retrieval algorithms

a. Description of IWRAP and HIWRAP

The IWRAP airborne Doppler radar was developed at the University of Massachusetts Microwave Remote Sensing Laboratory (UMASS – MiRSL) with the intention of studying high wind speed regions of intense atmospheric vortices such as hurricanes and winter storms. IWRAP is a dual-frequency (C- and Ku- band), dual-polarized (H/V), downward pointing and conically scanning (60 revolutions per minute; rpm) Doppler radar with up to four beams between ~ 30° – 50° incidence and 30 m range resolution. Typically, only two incidence angles are used for wind retrievals. Figure 1a shows the scanning geometry of IWRAP flying aboard the NOAA WP-3D aircraft, which has a typical flight altitude of ~ 2 – 4 km and an airspeed of ~ 100 – 150 m s^{-1} yielding along-track sampling by IWRAP of ~ 100 – 150 m. More details on IWRAP can be found in Fernandez et al. (2005).

The HIWRAP airborne Doppler radar was developed at the NASA Goddard Space Flight Center (GSFC) with the goal of studying hurricane genesis and intensification as well as other precipitating systems. One of the unique features of HIWRAP is its ability to fly on NASA's GH unmanned aircraft, which operates at ~ 18 – 20 km altitude and can remain airborne for more than 24 h. HIWRAP is a dual-frequency (Ku- and Ka- band), single-polarized (V for inner beam, H for outer beam), downward pointing and conically scanning (16 rpm) Doppler radar with two beams (~ 30° and 40°) and 150 m range resolution. Figure 1b shows the scanning geometry of HIWRAP aboard the NASA GH, which has an airspeed of ~ 160 m s^{-1} yielding ~ 600 m along-track sampling. More details on HIWRAP can be found in Li et al. (2008). Both radars complement each other well with IWRAP having little to no attenuation at C-band and very high sampling resolution capabilities while HIWRAP is able to measure the full troposphere, has a wider swath (~ 30 km vs. ~ 10 km for IWRAP, at the surface) and is able to detect light precipitation at Ka-band. In addition, both radars are able to derive ocean surface vector winds through scatterometry retrieval techniques.

b. Description of wind retrievals

Retrievals of the three Cartesian wind components over the entire viewing region or swath of IWRAP/HIWRAP can be performed using either a traditional least squares approach or through a variational procedure. In both approaches, the radar swath is divided up into discrete cells with horizontal grid spacing typically larger than the along-track sampling and vertical grid spacing consistent with the range resolution. Radial velocity observations (after being corrected for aircraft motions and velocity ambiguities) are assigned to each grid point by gathering data within an influence radius from the grid point. The level of smoothness desired in the wind vector solution, with larger radii allowing smoother solutions by attenuating high frequencies, dictates the choice of influence radius. The influence radii are discussed in detail in the next section.

Figure 2 summarizes the grid structure methodology described above for HIWRAP with 1 km x 1 km x 0.15 km grid cells. In Fig. 2, the outline of the conical scan (inner-beam at 30° and outer-beam at 40°) in track-relative coordinates is shown at the surface with the forward and backward portions of the scan labeled. The right side of Fig. 2 shows how radial velocity observations are assigned to each grid point with oversampling providing smoothing. The influence radii capture azimuth diversity in the radial velocities afforded by the intersections of the forward and backward portions of the conical scan. This azimuth diversity and the steep incidence angles of the radar beams are used to recover the three Cartesian wind components at each grid point. Note that the grid structure methodology shown in Fig. 2 is the same for IWRAP only the grid cells are typically 0.20 – 0.25 km in the horizontal and 0.03 km in the vertical.

Figure 3a illustrates the maximum azimuth diversity for the HIWRAP geometry and grid structure methodology outlined in Fig. 2 as a function of across track distance and height. For this calculation, simulated data is used (see section 3) and the influence radii are specified as a function of height with radii of ~ 4 km at the surface to ~ 1 km at 15 km height. The azimuth diversity for each grid point is computed by finding the largest azimuth difference between pairs of observations within the influence radii. Large values of azimuth diversity close to 90° (optimal for horizontal winds) are found in two patches ~ 5 – 7 km off nadir. Most of the swath has azimuth diversity near 80° with strong gradients that approach 40° at nadir where the diversity is smallest. Several Doppler radar studies have identified ~ 30° of azimuth diversity as a lower bound for determining reasonably accurate horizontal wind components (e.g. Klimowski and Marwitz 1992). The large values of azimuth diversity shown in Fig. 3a are possible because of the large, overlapping influence radii that are used to gather radar observations at each analysis grid point. However, as described in the next section, the observations in the influence radii are weighted based on the distance from the analysis grid point, which will produce somewhat smaller levels of azimuth diversity than those shown in Fig. 3a. Smaller influence radii will produce more narrow zones of large azimuth diversity with values that go below ~ 30° at nadir.

Figure 3b is the same as Fig. 3a, only the influence radii are ~ 1.8 km at the surface and decrease to ~ 0.8 km at 15 km height. The smaller influence radii decrease the azimuth diversity to a minimum of ~ 20° at nadir with the region of largest diversity confined to two thin bands between ± 5 – 10 km across-track. In addition, the edges of the radar swath have reduced azimuth diversity, which is due to the viewing geometry becoming collinear right along the swath edges (see Fig. 2). This edge effect does not appear in Fig. 3a because the influence radii are larger, which pulls in radial velocities from the swath interior that have larger azimuth diversity, resulting in larger maximum values. Despite this, the retrieved wind fields along the swath edges are still subject to the collinear nature of the viewing geometry due to the distance weighting in the solution procedure (see next section). Note that the results shown in Fig. 3 are nearly identical for IWRAP only the radar is typically located between 2 – 4 km heights.

i. The least squares approach

In the least squares approach, solutions for the wind components are found by solving a weighted least squares problem at each grid point,

$$\boldsymbol{J_o} = \|\boldsymbol{W}(\boldsymbol{f} - \boldsymbol{E}\boldsymbol{g})\|^2 \tag{1}$$

where $\boldsymbol{J_o}$ is termed the observation error cost function, $\boldsymbol{f}$ is a column vector of m Doppler velocity observations (after being corrected for aircraft motions, velocity ambiguities and hydrometeor fallspeeds) and $\boldsymbol{g} = [\mathrm{u\ v\ w}]^T$ is a column vector of the three unknown Cartesian wind components. The $\boldsymbol{W}$ in (1) is an $m \times m$ diagonal matrix of Gaussian weights with diagonal elements given by

$$W_i = exp\left(-\left[\frac{r_o^i}{\gamma\delta}\right]^2\right) \tag{2}$$

where r_o^i is the radius of the i^{th} observation from the analysis grid point, γ is a shape parameter that determines the width of the weighting function and δ is the influence radius expressed as

$$\delta = s\beta\left(1 - \frac{L_k}{H}\right) + s \tag{3}$$

where s is the along-track sampling of the radar, β is a chosen smoothing factor, L_k is the k^{th} vertical level of the analysis grid and H is the average height of the radar.

The smoothing factor (β) is a free parameter that determines the size of the influence radii. A larger value of β produces larger radii, which increases the number of points used to solve for the winds including oversampling with neighboring grid points (see Fig. 2). These smoothing effects result in an increase of the signal-to-noise ratio and accuracy of the wind vector solutions. However, larger values of β also decrease the effective resolution of the wind field analysis, where we define "effective resolution" as that radius where the weighting function in (2) reaches exponential decay (falls off to e^{-1}; e.g. Koch et al. 1983). The shape parameter (γ) has similar effects to β, determining the width of the filter response within the influence radius.

Wind vector solution sensitivity tests and spectral analysis (using simulated data described in section 3) with different values of β and γ indicated that a value of $\beta \approx 6$ and $\gamma = 0.75$ were reasonable (in terms of accuracy and damping characteristics) for this study. For a typical HIWRAP height of ~ 18 km and along-track sampling of ~ 0.6 km, values of the influence radii are ~ 4 km at the surface to ~ 1 km at 15 km height. This results in effective resolutions of ~ 3 km at the surface to just under 1 km at 15 km height. We chose to only use weights based on distance from the analysis grid point because, in theory, the estimated variance in the Doppler velocity observations is independent and constant. Reasor et al. (2009) and Lopez-Carrillo and Raymond (2011) also use a distance dependent weight in their retrieval algorithms.

Finally, in Eq. (1) ***E*** is an $m \times 3$ matrix of coordinate rotations to map the radar spherical coordinates to Cartesian space

$$\boldsymbol{E_{mx3}} = \begin{bmatrix} x_1 r_1^{-1} & y_1 r_1^{-1} & z_1 r_1^{-1} \\ \vdots & \vdots & \vdots \\ x_m r_m^{-1} & y_m r_m^{-1} & z_m r_m^{-1} \end{bmatrix} \qquad (4)$$

where r_m is the range for the m^{th} observation and the Earth-relative coordinates centered on the radar are given by (index subscript m dropped here for convenience)

$$\begin{pmatrix} x \\ y \\ z \end{pmatrix} = r \begin{pmatrix} \cos H\,(a) + \sin H \sin\tau\,(b) + \sin H\,(c) \\ -\sin H\,(a) + \cos H \sin\tau\,(b) + \cos H\,(c) \\ \sin\tau\,(\sin P \cos\theta - \cos P \sin R \sin\theta) - \cos P \cos R \cos\tau \end{pmatrix} \qquad (5)$$

where

$$\begin{pmatrix} a \\ b \\ c \end{pmatrix} = \begin{pmatrix} \cos R \sin\theta \sin\tau - \sin R \cos\tau \\ \cos P \cos\theta + \sin P \sin R \sin\theta \\ \sin P \cos R \cos\tau \end{pmatrix} \qquad (6)$$

and *P, R, θ*, *H* and τ are the pitch, roll, azimuth, heading and tilt angles, respectively. Equation (5) is derived for the IWRAP/HIWRAP geometry following Lee et al. (1994) and all angle conventions and coordinate systems follow this paper as well.

The unknown wind components $\boldsymbol{g}$ are found by solving the normal equations, which are formed by finding where the partial derivatives of $\boldsymbol{J_o}$ with respect to the unknown parameters (wind components) is equal to zero yielding

$$\boldsymbol{g} = (\boldsymbol{E^T W E})^{-1} \boldsymbol{E^T W f} \; . \tag{7}$$

Equation (7) is solved directly using a Cholesky decomposition/Gaussian elimination algorithm. Ray et al. (1978) and earlier papers such as Heymsfield (1976) were among the first studies to apply the basic formulation of the least squares approach for retrieving the Cartesian wind components from ground-based Doppler radar.

The main advantages of the least squares approach relative to the variational method (described next) are the computational efficiency (the setup and solution of Eq. (7) is done when assigning observations to each grid point, which takes a trivial amount of computer time) and the ability to analyze the theoretical uncertainty in the wind components through an error propagation analysis.

The general formula for error propagation is

$$\delta q^2 = \sum_i \left(\frac{\partial q}{\partial x_i} \delta x_i \right)^2 , \tag{8}$$

where δ*q* represents the Gaussian uncertainty in *q* (a function of x_i), and each x_i denotes a variable with associated uncertainty δx_i that contributes to the calculation of δ*q*. Applying Eq. (8) to Eq. (7) we obtain

$$\delta \boldsymbol{g}^2 = \boldsymbol{k k^T M}, \tag{9}$$

where $\boldsymbol{k} = (\boldsymbol{E^T W E})^{-1}\boldsymbol{E^T W}$ and $\boldsymbol{M} = \frac{\boldsymbol{J_o}}{\boldsymbol{d}}$ is the mean squared error of the weighted least squares fit with $\boldsymbol{d} = m - 3$ representing the degrees of freedom: the number of observations assigned to each grid point minus the number of estimated parameters (Cartesian wind components). In Eq. (9), the mean squared error is used to model the uncertainties in the Doppler velocity observations ($\delta \boldsymbol{f}$) because this quantity is more relevant to the theoretical treatment of the least squares parameter errors considered here (Strang 1986). By applying the matrix product identity on $\boldsymbol{k^T}$ in Eq. (9) we arrive at the final equation for the variance in the least squares estimated Cartesian wind components considered in this paper

$$\delta \boldsymbol{g}^2 = (\boldsymbol{E^T W E})^{-1}\boldsymbol{E^T W W^T E}(\boldsymbol{E^T W^T E})^{-1}\boldsymbol{M}. \tag{10}$$

A desirable feature of this error propagation analysis is the ability to analyze the errors in the retrieved wind components when no supporting data are available (the usual case). An examination of the usefulness of these fields will be presented in section 3a.

ii. The variational approach

The variational approach extends the least squares method by adding constraints to the basic observation error cost function shown in Eq. (1). Typically, these constraints include the anelastic mass continuity equation, which has been shown to improve retrievals of the vertical velocity (Gao et al. 1999), and a spatial filter to control noise (Sasaki 1970; Yang and Xu 1996). The cost function for our variational approach follows this tradition and takes the continuous form

$$\boldsymbol{J} = \boldsymbol{J_o} + \alpha_M \left\| \frac{\partial u}{\partial x} + \frac{\partial v}{\partial y} + \frac{1}{\rho}\frac{\partial \rho w}{\partial z} \right\|^2 + \alpha_S \|\nabla^2 \cdot \vec{v}\|^2, \tag{11}$$

where α_M and α_S are the weights for the anelastic mass continuity equation and the Laplacian spatial filter, respectively, $\rho = \rho(z)$ is an environmental density profile and $\vec{v}$ is the three-dimensional wind vector. The procedure for finding $\boldsymbol{g}$ in the variational approach initially proceeds the same as in the least squares method: take the partial derivatives of $\boldsymbol{J}$ with respect to $\boldsymbol{g}$ and set these equations equal to zero. However, instead of solving for $\boldsymbol{g}$ using linear algebra and a Gaussian elimination algorithm, $\boldsymbol{g}$ is found using an iterative, nonlinear conjugate gradient algorithm (we used CONMIN; Shanno 1978; Shanno and Phua 1980). A modern re-coding of CONMIN in Matlab was performed and the function [Eq. (11)] and gradient (not shown, but similar to Gao et al. 1999) evaluations are input to the algorithm for each iterative search for the minimum. The function and gradient evaluations are discretized to second-order accuracy.

The values of the weights are determined by trial-and-error using a numerical simulation of a hurricane (described in the next section) as truth. Values of $5\Delta x^2$ for α_M and $0 – O(\Delta x^4)$ for α_S are deemed reasonable where Δx^2 and Δx^4 are the square and fourth power of the horizontal grid spacing, respectively [a scaling to keep the units consistent with $\boldsymbol{J_o}$ in Eq. (11)]. A value of unity is used for the observation error term, $\boldsymbol{J_o}$.

Adding the mass continuity constraint reduced the error in the vertical velocity (relative to the least squares approach) by ~ 0.25 m s^{-1} on average. There were some regions where the reduction in the vertical velocity errors was larger, such as midlevel regions. The along-track winds did not change much with the addition of the mass continuity equation, but some small improvements were found in the across-track wind. Smoothing is already contained in the oversampling of observations used to solve the observation error term in Eq. (11), so values of α_S near 0 were sufficient for the simulated data with ± 1 – 2 m s^{-1} random noise. For measured radar observations with significant noise, the Laplacian filter is more important ($\alpha_S \sim \Delta x^4$) to enable convergence of the minimization algorithm and for obtaining reasonably smooth solutions.

We choose not to discuss the details of the variational solution results because the differences with the least squares results are minimal with the exception of some improvements in the vertical and across-track winds. The incidence angles of IWRAP and HIWRAP are steep and ~ 77 – 87 % (for incidence angles between 30 – 40°) of the true vertical velocity is measured resulting in relatively small errors in the retrieved vertical velocity over the inner portion of the radar swath (~ ± 5 km from nadir). Consequently, the mass continuity constraint will tend to have less impact on reducing the vertical velocity errors than other airborne radars (such as ELDORA) that scan at larger incidence angles and therefore measure less of the vertical velocity.

3. Error characteristics

A numerical simulation of Hurricane Bonnie (1998) at 2 km horizontal and ~ 0.65 km vertical (27 levels) resolutions described in Braun et al. (2006) was used to study the error characteristics of the wind retrieval algorithms. For this simulator we have focused on the HIWRAP radar, but because the scanning geometry and retrieval methods are the same, the errors for IWRAP will be similar. The numerical simulation revealed a realistic, environmental wind shear induced, wavenumber-one asymmetry in the storm core with embedded deep convective towers and mesovortices (see Braun et al. 2006 for displays of the storm structure). These structures are common in nature and they provide a good test case for evaluating the performance of the wind retrieval algorithms.

The simulated storm is repositioned in the center of the model domain (2 km resolution portion covers ~ 450 km^2) to allow for the use of a storm-centered retrieval grid. The GH aircraft is initialized in a portion of the domain and characteristic HIWRAP scan parameters are set as follows: two beams (30° and 40° incidence), 2° azimuthal sampling, 0.60 km along-track sampling (based on an airspeed of 160 m s^{-1}) and 0.15 km gate spacing. The GH attitude parameters are taken from real data during flights over TCs during GRIP. The mean and standard deviation of the aircraft attitude parameters are: altitude (18.5 km ± 0.1), pitch (2.5° ± 0.5) and roll (0° ± 0.5). Random perturbations with a uniform distribution and upper limits dictated by the standard deviations are added to the mean values of the attitude parameters in the code.

The Bonnie simulated wind fields (u, v and w) are interpolated to the radar points and the radial velocities are calculated

$$V = (ux + vy + wz)r^{-1} \tag{12}$$

where x, y and z are given in Eq. (5). The hydrometeor fallspeed is set to zero when computing the radial velocities. Random errors of ± 1 – 2 m s^{-1} with a uniform distribution were added to the radial velocities to simulate the typical uncertainties of measured Doppler velocities from IWRAP and HIWRAP with signal-to-noise ratios of ~ 10 dB or larger (typical of the hurricane eyewall; Fernandez et al. 2005). Larger errors are considered to examine the robustness of the retrieval statistics and will be noted where appropriate. Note that measured Doppler velocities encompass a number of systematic errors (e.g. aliasing, antenna pointing errors, beam filling issues) that are not addressed with the simulator.

A retrieval grid centered on the storm center that covers 250 km^2 in the horizontal with 2 km grid spacing (to match the numerical simulation) and 15 km in the vertical with 1 km grid spacing (an extra level at 0.5 km was added to sample winds in the boundary layer) was created. The three Cartesian velocity components are then computed on this grid using the least squares and variational retrieval methods.

Three aircraft flight patterns were considered for the simulator: (1) a straight-line segment ~ 200 km in length in a weaker portion of the model domain with maximum winds of ~ 30 m s^{-1}, (2) a straight line segment ~ 200 km in length across the eyewall of Bonnie with maximum winds of ~ 60 m s^{-1} and (3) a 1.8 h rotated figure four pattern centered on the storm center with ~ 100 km radial legs. The rotated figure four is the most common TC flight pattern for the IWRAP and HIWRAP radars. The qualitative structure of the root mean square errors (RMSEs) for each wind component were similar for the weak and eyewall flight segment so we focus here on the eyewall segment because the sharp gradients of the eyewall are more challenging for the retrieval algorithms. All retrieval results shown are from the least squares method.

a. Eyewall flight segment

Figure 4a shows the zonal (across-track) velocity field for the simulated truth field at 1 km height for a northerly GH heading across the simulated eyewall of Bonnie at 1200 UTC 23 August 1998 with maximum zonal wind speeds of ~ 60 m s^{-1}. The retrieved zonal wind speeds along with the RMSEs at 1 km height are shown in Fig. 4b. The RMSEs are typically largest (> 6 m s^{-1}) at the junction between the inner edge of the eyewall and the edge of the swath. This structure is due to the sharp gradients of the eyewall interface, which are difficult to capture, and the poor azimuth diversity that occurs right along the edges of the radar scan (see discussion of Fig. 3 in section 2b). The least squares solution for the wind field incorporates all observations in the influence radius with largest weight given to those observations closest to the analysis grid point. This leads to a greater chance for errors and potentially unstable solutions along the swath edges. Away from the edges and the inner edge of the eyewall, the RMSEs in Fig. 4b are mostly 2 – 4 m s^{-1} even in the core of the eyewall where the wind speeds are large. Note that across-track winds can be retrieved at nadir because the influence radii at nadir grid points allow for enough azimuth diversity (see Fig. 3) to compute the horizontal wind vector.

Figures 5a and 5b show vertical cross sections at nadir of the across-track velocity from the simulated truth and retrievals, respectively. The main structural features of the simulated truth field, such as the radius of maximum winds, eyewall slope and decay of winds with height, are captured well by the retrievals. The majority of the errors are ~ 2 – 4 m s^{-1} in the core of the eyewall (~ ± 40 – 60 km along-track) with lower values outside of this region. The largest errors of ~ 6 m s^{-1} occur mostly in the boundary layer and on the southern side of the storm (around -50 km along-track) in a few patches extending from low levels up to ~ 10 km height.

Figure 6a shows the RMSEs for the across-track velocity averaged along-track for the eyewall flight segment. This figure (and subsequent plots for the other wind components) is intended to summarize the error structure of the downward pointing, conically scanning radar. The largest RMSEs of 5 m s^{-1} or greater occur in the boundary layer where the wind speeds and gradients in the eyewall are large. Above ~ 1 km height, the RMSEs are largely 2 – 3 m s^{-1} with lowest values of ~ 1 m s^{-1} found above 10 km height. There are also indications of larger errors at the swath edges in Fig. 6a, consistent with Fig. 4 and associated discussion.

A more revealing error diagnostic for each velocity component is the relative RMSE (REL) expressed as

$$REL = \left[\frac{\sum_{i=1}^{n}\left(X_i^T - X_i^R\right)^2}{\sum_{i=1}^{n}\left(X_i^T\right)^2}\right] \times 100 \qquad (13)$$

where X_i^T is the model truth velocity component for each grid point *i*, X_i^R is the retrieved velocity component and *n* is the number of grid points. Figure 6b shows the RELs for the eyewall flight segment with the summations in Eq. (13) taken over the along-track grid points. The RELs in Fig. 6b are able to put the RMSEs in Fig. 6a into perspective, which is useful for understanding and generalizing the results. Above ~ 1 km height, the REL values are ~ 10 – 12 % on many of the swath edges and ~ 5 – 8 % everywhere else in the swath with the lowest values of ~ 5 % found above 10 km height consistent with Fig. 6a. The errors are lowest at upper levels because the azimuth diversity is maximized there since all the radar-viewing angles collapse to one or two grid points (see Fig. 3).

Figure 7a shows the meridional (along-track) velocity for the same flight track as in Fig. 4 at 1 km height. The maximum meridional wind speed in this section of Bonnie's eyewall is ~ 20 m s^{-1}. Figure 7b reveals that the along-track winds have very small RMSEs with largest values of 0.5 – 1.0 m s^{-1} on the swath edges and values of 0.25 m s^{-1} or lower in the interior of the swath. This across-track structure for the along-track velocity can be understood by referring back to the COPLAN wind retrieval method described in the introduction. At nadir, the radar beams sample little across-track velocity and the along-track velocity can, in theory, be solved for exactly (Tian et al. 2011 discuss the COPLAN method applied to HIWRAP). As the radar beams scan away from nadir, more across-track velocity is sampled and the along-track wind errors increase. The error structure is similar at other levels and is not shown. Instead, to illustrate the vertical structure of the along-track winds, a vertical cross-section comparison is shown at nadir.

Figures 8a and 8b show the simulated truth and retrieved along-track winds at nadir, respectively. There is almost an exact match between the simulated truth and the retrieval fields with the only discernable errors, which are very small (largely 0.25 m s^{-1} or less), occurring at or below 5 km height especially on the southern side of the storm. There is also a region of 0.25 m s^{-1} errors right along the edge of the eyewall sloping outward with height on both sides of the storm between ~ 40 – 80 km along track.

Figure 9 shows the along-track averaged errors for the along-track velocity. The RMSEs in Fig. 9a reveal clear across-track dependence at all levels with lowest errors at nadir, which was also seen in Figs. 7b and 8b. The largest errors are only ~ 1 m s^{-1} at the swath edges below ~ 5 km height with the majority of the swath having RMSEs of ~ 0.25 m s^{-1}. The RELs in Fig. 9b show large pockets with errors of only ~ 2 %. Even though the RMSEs are only 1 m s^{-1} at the swath edges, the RELs put this into perspective by revealing some larger values of ~ 15 % or greater in some spots. Overall, however, the RELs are still quite low with the majority of the swath having values less than 10 %.

Finally, moving on to the vertical velocity, Fig. 10 shows horizontal cross sections of vertical velocity at 8 km height. In the southern eyewall section of the simulated truth (Fig. 10a), a pronounced updraft/downdraft couplet with values of ~ 4 m s^{-1} is visible. The corresponding retrieval vertical velocities in Fig. 10b capture this structure fairly well over most of the swath (especially at nadir), but larger errors of 0.5 – 1.0 m s^{-1}

distort the retrieved vertical velocities towards the swath edges. In the northern section of the eyewall, larger errors at the swath edges are also apparent with the smallest errors of less than 0.5 m s^{-1} centered on the middle part of the swath.

Figure 11 shows the vertical structure of the vertical velocities at nadir from the simulated truth and the retrievals. The small errors at nadir shown in Fig. 10 are made very clear with the structural comparison in Fig. 11. There is a very close match between the simulated truth and the retrieval fields with the only discernable errors, which are small (0.25 m s^{-1}), occurring at the locations of the maximum updrafts as well as in the boundary layer. Off-nadir vertical cross section comparisons of the vertical velocity (not shown) were also analyzed and the core updraft/downdraft features are well resolved out to approximately ± 5 km from nadir with some larger errors present. Beyond ± 5 – 6 km across-track, errors in the vertical velocity structure become larger as shown in Fig. 10.

Figure 12 shows the along-track averaged errors for the vertical velocity. The RMSEs in Fig. 12a have strong across-track dependence with lowest errors (~ 0.25 m s^{-1}) at nadir and largest errors (~ 3 – 5 m s^{-1}) at the swath edges. This across-track structure is due to the same reasoning as that described for the along-track velocity above. That is, the solutions for the vertical velocity field described in this paper are approximations to the COPLAN method, which yields an exact expression for the vertical velocity at nadir. As the radar beams scan away from nadir, more across-track velocity is sampled and the vertical velocity errors increase. The RELs in Fig. 12b are very useful for placing the vertical velocity RMSEs in perspective. At nadir the REL values are ~ 25 %, which is excellent, and increase to several hundred percent at the swath edges below ~ 5 km height. Above ~ 5 km height, the RELs are lower with the 100 – 150 % contour extending out to the edges of the swath. The lower RELs above ~ 5 km height reflects the larger vertical velocities and smaller horizontal velocities at these levels.

The simulated errors presented in this section are a useful guide to the expected errors in the retrieved Cartesian wind components when using measured data. However, measured Doppler velocities can encompass more complicated random errors (e.g. noise structure, missing data) and varying environmental flow scenarios that limit the use of simulated errors. The theoretical error propagation analysis derived in section 2c for the least squares approach is intended to provide error guidance when using measured Doppler velocity data and will be analyzed in section 4. Below, we briefly describe the correlation between the simulated and theoretical errors as an initial assessment of their value.

Figure 13 shows the standard deviations of the Cartesian wind components using the error propagation analysis. Figures 13a, 13b and 13c show the across-track, along-track and vertical standard deviations, respectively for the same levels and flight track as in Figs. 4b, 7b and 10b. The standard deviations are computed by taking the square root of the diagonal elements of $\delta \boldsymbol{g}^2$ in Eq. (10). The spatial structure of the theoretical errors is highly correlated with the simulated errors including regions of maximum/minimum values and the strong across-track dependence of the errors for the along-track and vertical components (compare Figs. 4b, 7b and 10b with Figs. 13a, 13b and 13c, respectively). The magnitudes of the theoretical errors are typically lower than those for the corresponding simulated errors especially for the across-track velocity. This is probably due to the fact that the simulated errors are more connected to the actual structure of the flow field whereas the theoretical errors attempt to predict these errors by accounting for the quality of the least squares fit and the scanning geometry including the weighting function. We believe the theoretical errors are still quite useful and can be regarded as a somewhat lower estimate of the true errors.

b. Rotated figure-four flight pattern

Figure 14 shows a 1.8 h rotated figure-four flight pattern (100 km radial legs) of the simulated Bonnie at 1 km height starting at 1200 UTC 23 August sampled by HIWRAP. This figure is intended to illustrate the spatial coverage of retrieval winds and reflectivity afforded by HIWRAP for the common rotated figure-four pattern executed during the NASA GRIP field experiment (Braun et al. 2013).

Table 1 presents a summary of the Cartesian velocity retrieval errors averaged over the HIWRAP sampling volume for this flight pattern. Results from three experiments with different random error perturbations added to the simulated Doppler velocities are shown: ± 1 – 2 m s^{-1} (ERR1; default case), ± 2 – 4 m s^{-1} (ERR2) and ± 4 – 8 m s^{-1} (ERR3). Table 1 shows that the low horizontal wind component errors are relatively robust to large random errors in the Doppler velocity. Increases of only ~ 1 m s^{-1} in RMSE and ~ 4 % in REL are found for the horizontal wind components when adding the largest error perturbations (± 4 – 8 m s^{-1}). The vertical wind component is more sensitive to random errors. Although the RMSEs only increase by ~ 0.75 m s^{-1} for the largest error perturbations, this is significant as REL values increase by ~ 75 % and the correlation coefficient decreases from 0.42 to 0.29. The vertical velocity errors presented in Table 1 may seem large; this is due to averaging the errors over the entire radar sampling volume. However, as shown in Fig. 12, there is strong across-track dependence in the vertical velocity errors. Therefore, if one focuses on the middle portion of the radar swath (approximately ± 5 km from nadir), substantial reductions in vertical velocity errors can be achieved.

4. Example wind retrievals from measured data

In this section, we illustrate the utility of the wind retrieval algorithms (least squares method) for analyzing hurricanes using measured data collected by IWRAP and HIWRAP. We first show nadir wind retrievals using IWRAP data collected in Hurricane Isabel (2003) on September 12 from 1900 – 1930 UTC. During this time period, Isabel was maintaining category five intensity with a minimum surface pressure of ~ 920 hPa and maximum sustained winds of ~ 72 m s^{-1} (~ 160 miles per hour).

Figure 15 shows a horizontal cross section (~ 2 km height) of radar reflectivity (C band) in Hurricane Isabel at ~ 1900 UTC September 12, 2003 from the lower fuselage radar on the NOAA P3 aircraft. There is a concentric eyewall present in Isabel at this time with an outer eyewall at a radius of ~ 60 km from the storm center and an inner eyewall at ~ 30 km radius. The black arrow in Fig. 15 shows an outbound flight segment where the NOAA P3 aircraft (with IWRAP mounted underneath) penetrated the inner eyewall of Isabel and approached the outer eyewall.

Figure 16a shows a vertical cross-section of IWRAP reflectivity at C band along the black arrow illustrated in Fig. 15. The IWRAP reflectivity is mapped to a grid with horizontal grid spacing of 0.25 km and vertical grid spacing of 30 m. The wind retrievals use this same grid only the vertical grid spacing is set to 100 m. Data below ~ 0.40 km height is removed due to contamination by ocean surface scattering entering through the radar's main lobe. The inner eyewall of Isabel is centered at ~ 35 km along track in Fig.

16a with peak reflectivities of ~ 50 dBZ at C band. Reflectivity oscillations (bands of enhanced and depressed reflectivity) with wavelengths of ~ 2 – 4 km are located radially outside the inner eyewall of Isabel from ~ 40 – 60 km along track.

Figure 16b shows the retrieved horizontal wind speeds at nadir using the least squares method and the C band Doppler velocities (Nyquist interval of ~ ± 225 m s^{-1}) with rain fallspeeds calculated according to Ulbrich and Chilson (1994) and Heymsfield et al. (1999). To address noise in the data and calculations, Doppler velocities with pulse pair correlation coefficient (PPCC) values below 0.25 were removed and the smoothing factor (β) in Eq. (3) was increased to 7. The inner eyewall of Isabel is intense with maximum wind speeds of ~ 80 m s^{-1} and average values of 65 – 70 m s^{-1}. These estimates match well with flight level data from the NOAA N42 aircraft. Radially outside the inner eyewall, oscillations in the wind speeds are consistent with the reflectivity structure in Fig. 16a.

Figure 16c shows the retrieved vertical winds at nadir with the same data processing and quality control as the horizontal winds. The core of the inner eyewall (centered at 35 km along track) is dominated by a broad region of downward motion with maximum values between ~ -3 and -5 m s^{-1}. A strong updraft sloping radially outward with height is located on the inner edge of the primary eyewall with values between 5 – 15 m s^{-1}. These calculations also match reasonably well with the flight level data. The hurricane structure is consistent with a concentric eyewall cycle (e.g. Willoughby et al. 1982) occurring within Isabel at this time. In the region between the inner and outer eyewall (~ 40 – 60 km along track), there are oscillations in vertical velocity that are well correlated with the oscillations in the reflectivity structure shown in Fig. 16a. This suggests some type of wave is propagating radially outward away from the inner eyewall and towards the outer eyewall.

We now illustrate retrievals of the horizontal wind vector for HIWRAP observations of Tropical Storm Matthew (2010) during the NASA GRIP field experiment. Figure 17 shows a GOES infrared image of Matthew on September 24 at 0645 UTC overlaid with the GH track. During this time period, Matthew was a weak tropical storm with a minimum surface pressure of 1003 hPa and maximum sustained winds of ~ 23 m s^{-1} with vertical wind shear from the northeast at 10 – 15 m s^{-1}. Despite the significant vertical wind shear, Matthew was intensifying steadily with convective bursts (shown by the brightness temperatures between 185 – 190 K in Fig. 17) located in the down shear portions of the storm. The blue highlighted lines in Fig. 17 denote HIWRAP flight segments analyzed.

Figure 18 shows retrievals of the horizontal wind vector overlaid on Ku band reflectivity at 3 km height for the three blue flight segments highlighted in Fig. 17 between 0552 – 0742 UTC on September 24. The retrieval grid is Lagrangian, following the National Hurricane Center (NHC) estimate of the center of Matthew at the middle of each flight segment, with a grid spacing of 1 km.

The GRIP experiment was the first time HIWRAP collected significant data and some issues with the data (e.g. excessive noise and problems with dealiasing Doppler velocities) were found. To address these issues, we have done two things: (1) pulse pair estimates were reprocessed with 128 pulses averaged, which improves the signal-to-noise ratio as well as the performance of the dual pulse repetition frequency dealiasing calculation and (2) Doppler velocities below the noise saturation threshold (determined using a power threshold, which translates to ~ 25 dBZ at 3 km height) were removed. The smoothing factor (β) in Eq. (3) was set to 6 in the swath interior and ~ 7 on the swath edges. Hydrometeor fallspeeds are removed from the data using the rain relations described in Ulbrich and Chilson (1994) and Heymsfield et al. (1999).

A clear cyclonic circulation is evident in Fig. 18 with a center of circulation ~ 50 km W to NW of the center estimate from the NHC at x ~ -45 km, y ~ 23 km. The strongest winds of 25 – 35 m s^{-1} are located to the North of the HIWRAP derived circulation center coincident with deep convective towers. Deep convective towers are also present to the southwest of the HIWRAP center embedded within the partial eyewall shown by the strong reflectivity gradients and curved flow (x ~ -70 km, y ~ 0 km). The wind speeds in this section are ~ 10 m s^{-1} on average with stronger winds of 15 – 20 m s^{-1} connected with the deep convection (high reflectivity regions).

Figure 19 shows the standard deviations in the wind speeds (described in section 2c) for the HIWRAP composite analysis shown in Fig. 18. The standard deviations are computed by taking the square root of the diagonal elements of $\delta\boldsymbol{g}^2$ in Eq. (10). This produces a standard deviation for each wind component and we have taken the magnitude of the horizontal standard deviations to summarize the errors in the horizontal winds. The wind speed errors are the smallest (~ 0.5 m s^{-1}) in the middle section of each swath and increase toward the swath edges (~ 1 – 2 m s^{-1}). These results are consistent with the error analysis described in section 3. The largest errors of ~ 3 – 5 m s^{-1} occur in the Northern section of the analysis (especially along the edges) where the wind speeds are strongest. These errors, derived from a propagation analysis, are useful for providing an estimate of the errors in the computed winds by taking into account the radar geometry and quality of the least squares fit to the observations.

5. Summary and conclusions

In this paper, algorithms for the retrieval of atmospheric winds in precipitating systems from downward pointing, conically scanning airborne Doppler radars was presented with a focus on the IWRAP and HIWRAP systems. Retrievals of the three Cartesian wind components over the entire radar sampling volume are described, which can be determined using either a traditional least squares or variational solution procedure.

The random errors in the retrievals are evaluated using both an error propagation analysis with least squares theory and a numerical simulation of a hurricane. These error analyses show that the along-track and vertical wind RMSEs have strong across-track dependence with values of ~ 0.25 m s^{-1} at nadir to ~ 1.00 m s^{-1} and ~ 2.00 m s^{-1} at the swath edges, respectively. The across-track wind errors have a more complicated distribution, but in general get larger at the swath edges, which is due to the radar viewing geometry becoming collinear along the swath edges. On average, the across-track wind errors are ~ 3.40 m s^{-1} or 10% of the local wind speed. In the center of the radar swath away from the eyewall edges, the across-track wind errors are ~ 2 – 3 m s^{-1}. For typical rotated figure four flight patterns through hurricanes, the zonal and meridional wind speed errors are ~ 2 – 3 m s^{-1} or 9 – 14 % of the local wind speed depending on the amount of noise added to the Doppler velocities.

Both the traditional least squares and variational methods are able to provide the three Cartesian wind components over the entire swath at reasonably high resolution with the effective resolution dictated by the chosen smoothing and weighting parameters. Both methods can provide good accuracy of the horizontal winds across most of the swath and vertical winds within ± 5 – 6 km of nadir. For the least squares method, one of the unique positive attributes is the ability to analyze the theoretical uncertainties in the wind components through an error propagation analysis. One unique drawback of the least squares method is the inability to consider dynamic constraints on the wind field such as mass continuity, which was found to slightly reduce the errors in the vertical and across-track winds with the variational solution procedure. However, problems with convergence of the variational solutions for noisy data and increased computer time relative to the least squares method are drawbacks of the variational method.

A major science motivation for the IWRAP and HIWRAP airborne radars is the study of hurricanes. Examples of measured data wind retrievals from IWRAP during an eyewall replacement cycle in Hurricane Isabel (2003) and from HIWRAP during the development of Tropical Storm Matthew (2010) were shown. These high-resolution measurements, especially for IWRAP, along with the dual-frequency nature of both radars and the long sampling times of HIWRAP from the NASA Global Hawk aircraft provide a unique ability to address important hurricane science questions. A detailed science analysis of the IWRAP and HIWRAP data associated with these wind retrieval examples is warranted and will be reported in a forthcoming paper.

Acknowledgments. We would like to thank Matt McLinden for his feedback on the HIWRAP data as well as his engineering efforts. We also thank Dr. Lihua Li, Martin Perrine, Jaime Cervantes and Ed Zenker for their engineering work with the HIWRAP radar. A thanks also goes out to Dr. Jim Carswell for discussions and support of the IWRAP work. The majority of this research was carried out when the first author was a postdoctoral fellow through the NASA Postdoctoral Program (NPP) stationed at Goddard Space Flight Center. Steve Guimond thanks NPP for their support of this work.

REFERENCES

Armijo, L., 1969: A theory for the determination of wind and precipitation velocities with Doppler radars. *J. Atmos. Sci.*, **26,** 570 – 575.

Bell, M.M., M.T. Montgomery, and K.A. Emanuel, 2012: Air-sea enthalpy and momentum exchange at major hurricane wind speeds observed during CBLAST. *J. Atmos. Sci.*, **69,** 3197 – 3222.

Bohne, A.R., and R.C. Srivastava, 1975: Random errors in wind and precipitation fall speed measurements by a triple Doppler radar system. *Preprints, 17th Conf. Radar Meteorology*, Seattle, WA, Amer. Meteor. Soc., 7 – 14.

Braun, S., R. Kakar, E. Zipser, G. Heymsfield, C. Albers, S. Brown, S. Durden, S. Guimond, J. Halverson, A. Heymsfield, S. Ismail, B. Lambrigtsen, T. Miller, S. Tanelli, J. Thomas and J. Zawislak, 2013: NASA's Genesis and Rapid Intensification Processes (GRIP) field experiment. *Bull. Amer. Meteor. Soc.*, **94,** 345 – 363.

_____, M. Montgomery, and Z. Pu, 2006: High-resolution simulation of Hurricane Bonnie (1998). Part I: The organization of eyewall vertical motion. *J. Atmos. Sci.*, **63,** 19 – 42.

Chong, M., and C. Campos, 1996: Extended overdetermined dual-Doppler formalism in synthesizing airborne Doppler radar data. *J. Atmos. Oceanic Technol.*, **13,** 581 – 597.

Fernandez, D.E., E. Kerr, A. Castells, S. Frasier, J. Carswell, P.S. Chang, P. Black, and F. Marks, 2005: IWRAP: The Imaging Wind and Rain Airborne Profiler for remote sensing of the ocean and the atmospheric boundary layer within tropical cyclones. *IEEE Trans. Geosci. Remote Sens.,* **43,** 1775 – 1787.

Gamache, J.F., F.D. Marks, and F. Roux, 1995: Comparison of three airborne Doppler sampling techniques with airborne in situ wind observations in Hurricane Gustav (1990). *J. Atmos. Oceanic Technol.*, **12,** 171 – 181.

Gao, J., M. Xue, A. Shapiro, and K.K. Droegemeier, 1999: A variational method for the analysis of three-dimensional wind fields from two Doppler radars. *Mon. Wea. Rev.*, **127,** 2128 – 2142.

Heymsfield, G.M., 1976: Statistical objective analysis of dual-Doppler radar data from a tornadic storm. *J. Appl. Meteor.*, **15,** 59 – 68.

_____, and Coauthors, 1996: The EDOP radar system on the high-altitude NASA ER-2 aircraft. *J. Atmos. Oceanic Technol.*, **13,** 795 – 809.

_____, J.B. Halverson, and I.J. Caylor, 1999: A wintertime Gulf Coast squall line observed by EDOP airborne Doppler radar. *Mon. Wea. Rev.*, **127,** 2928 – 2950.

Hildebrand, P.H., and Coauthors, 1996: The ELDORA/ASTRAIA airborne Doppler weather radar: High-resolution observations from TOGA COARE. *Bull. Amer. Meteor. Soc.*, **77,** 213 – 233.

Klimowski, B.A., and J.D. Marwitz, 1992: The synthetic dual-Doppler analysis technique. *J. Atmos. Oceanic Technol.*, **9,** 728 – 745.

Koch, S.E., M. desJardins, and P.J. Kocin, 1983: An interactive Barnes objective map analysis scheme for use with satellite and conventional data. *J. Climate Appl. Meteor.*, **22,** 1487 – 1503.

Lee, W.C., P. Dodge, F.D. Marks Jr., and P.H. Hildebrand, 1994: Mapping of airborne Doppler radar data. *J. Atmos. Oceanic Technol.*, **11,** 572 – 578.

Lhermitte. R.M., 1970: Dual-Doppler radar observations of convective storm circulation. *Prepr, Radar Meteorol. Conf., 14th, 1970* pp. 153 – 156.

Li, L., G.M. Heymsfield, J. Carswell, D. Schaubert, J. Creticos, M. Vega, 2008: High-altitude Imaging Wind and Rain Airborne Profiler (HIWRAP), Proceedings of IGARSS 2008 (IEEE International Geoscience & Remote Sensing Symposium), Boston, MA, USA, July 6 – 11, 2008.

Lopez-Carrillo, C., and D.J. Raymond, 2011: Retrieval of three-dimensional wind fields from Doppler radar data using an efficient two-step approach. *Atmos. Meas. Tech.*, **4,** 2717 – 2733.

Marks, F.D., and R.A. Houze, 1984: Airborne Doppler radar observations in Hurricane Debby. *Bull. Amer. Meteor. Soc.,* **65,** 569 – 582.

_____, R.A. Houze, and J. Gamache, 1992: Dual-aircraft investigation of the inner core of Hurricane Norbert: Part I: Kinematic structure. *J. Atmos. Sci.*, **49,** 919 – 942.

Matejka, T., and D.L. Bartels, 1998: The accuracy of vertical air velocities from Doppler radar data. *Mon. Wea. Rev.,* **126,** 92 – 117.

Ray, P.S., K.K. Wagner, K.W. Johnson, J.J. Stephens, W.C. Baumgarner, and E.A. Mueller, 1978: Triple-Doppler observations of a convective storm. *J. Appl. Meteor,* **17,** 1201 – 1212.

_____, C.L. Ziegler, W. Bumgarner, and R.J. Serafin, 1980: Single- and multiple-Doppler radar observations of tornadic storms. *Mon. Wea. Rev.,* **108,** 1607 – 1625.

Reasor, P.D., M.D. Eastin, and J.F. Gamache, 2009: Rapidly intensifying Hurricane Guillermo (1997). Part I: Low-wavenumber structure and evolution. *Mon. Wea. Rev.*, **137,** 603 – 631.

Sasaki, Y., 1970: Some basic formalisms in numerical variational analysis. *Mon. Wea. Rev.*, **98,** 875 – 883.

Shanno, D.F., 1978: Conjugate gradient methods with inexact searches. *Math. Operations Res.*, **3,** 244 – 256.

_____, and K.H. Phua, 1980: Remark on algorithm 500 – a variable method subroutine for unconstrained nonlinear minimization. *ACM Trans. on Mathematical Software,* **6,** 618 – 622.

Strang, G., 1986: *Introduction to Applied Mathematics*. Wellesley-Cambridge Press.

Testud, J., and M. Chong, 1983: Three-dimensional wind field analysis from dual-Doppler radar data. Part I: Filtering, interpolating and differentiating the raw data. *J. Climate Appl. Meteor.*, **22,** 1204 – 1215.

Tian, L., G. Heymsfield, S. Guimond, L. Li, and R. Srivastava, 2011: 3D wind retrieval from downward conical scanning airborne Doppler radar. *Proc. 35th Conf. Radar Meteorology*, Pittsburgh, PA, Amer. Meteor. Soc., 7 pp.

Ulbrich, C.W., and P.B. Chilson, 1994: Effects of variations in precipitation size distribution and fallspeed law parameters on relations between mean Doppler fallspeed and reflectivity factor. *J. Atmos. Oceanic Technol.*, **11,** 1656-1663.

Willoughby, H.E., J.A. Clos, and M.G. Shoreibah, 1982: Concentric eyewalls, secondary wind maxima, and the evolution of the hurricane vortex. *J. Atmos. Sci.*, **39,** 395-411.

Yang, S. and Q. Xu, 1996: Statistical errors in variational data assimilation – A theoretical one-dimensional analysis applied to Doppler wind retrieval. *J. Atmos. Sci.*, **53,** 2563 – 2577.

Ziegler, C.L., 1978: A dual Doppler variational objective analysis as applied to studies of convective storms. Master's thesis, University of Oklahoma, 115 pp.

TABLE CAPTIONS

1. Summary of HIWRAP velocity retrieval (using least squares method) errors for the Hurricane Bonnie (1998) simulated 1.8 h rotated figure-four flight pattern shown in Fig. 14. See text for details. The RMSEs are expressed in m s^{-1} and the RELs in % (rounded to the nearest whole number). The variable R is the correlation coefficient.

FIGURE CAPTIONS

1. Measurement geometry for (a) IWRAP aboard the NOAA WP-3D aircraft with typical flight altitudes of ~ 2 – 4 km and (b) HIWRAP aboard the NASA Global Hawk aircraft with typical flight altitudes of ~ 18 – 20 km.

2. Scan pattern and grid structure methodology for HIWRAP. The forward and backward portions of the scan are labeled in blue and red, respectively. The inner beam (30°) and outer beam (40°) are shown in dashed and solid lines, respectively. The influence radii shown are only 1 km for illustration, but are larger for calculations. See text for more details.

3. Maximum azimuth diversity in degrees for the HIWRAP geometry and grid structure methodology outlined in Fig. 2 only the influence radii are (a) ~ 4 km at the surface to ~ 1 km at 15 km height and (b) ~ 1.8 km at the surface to ~ 0.8 km at 15 km height. Note the color bar is different in each figure. See text for details.

4. Simulated HIWRAP zonal (across-track) velocity at 1 km height for a northerly GH track across the eyewall of Hurricane Bonnie (1998) at 1200 UTC 23 August. The shading shows (a) the model truth field and (b) the retrieval field with the black contours revealing the RMSEs with a contour interval of 2 m s^{-1} from 2 – 10 m s^{-1}. Fields are only shown where the simulated reflectivity is greater than 0 dBZ.

5. Comparison of (a) simulated truth and (b) retrieved zonal (across-track) velocity structure at nadir for the eyewall flight segment described in the text. The black contours in (b) show the RMSEs at 2, 4 and 6 m s^{-1}. Note that no reflectivity mask is applied to these fields and the vertical axis is exaggerated to show detail.

6. Simulated HIWRAP zonal (across-track) velocity retrieval errors for the same flight track as that shown in Fig 4. In these figures, the averages are taken in the along-track direction. The shading shows the (a) RMSEs and (b) RELs.

7. Same as in Fig. 4 only for the meridional (along-track) velocity with black error contours in (b) from 0.25 – 1.0 m s^{-1} with a 0.25 m s^{-1} interval.

8. Same as in Fig. 5 only for the meridional (along-track) velocity. The black contours in (b) show the RMSEs at 0.25 and 0.50 m s^{-1}.

9. Same as in Fig. 6 only for the meridional (along-track) velocity.

10. Same as in Fig. 4 only for the vertical velocity at 8 km height with the black error contours in (b) drawn at 0.5 and 1.0 m s^{-1}.

11. Same as in Fig. 5 only for the vertical velocity. The black contours in (b) show the RMSEs at 0.25 m s^{-1}.

12. Same as in Fig. 6 only for the vertical velocity.

13. Standard deviations of the Cartesian wind components using an error propagation analysis with least squares theory (see text for details). The figures are (a) zonal (across-track) velocity at 1 km height (b) meridional (along-track) velocity at 1 km height and (c) vertical velocity at 8 km height. Note the different x-axis scale for the vertical velocity figure.

14. HIWRAP 1.8 h rotated figure-four sampling of the Bonnie numerical simulation at 1 km height starting at 1200 UTC 23 August 1998. In this figure, the winds are from the least squares retrieval method. The shading is simulated reflectivity in dBZ and the reference arrow at (-80, -80) is 50 m s^{-1}. The large hole (no reflectivity/winds) in the center is the large eye of the simulated Bonnie.

15. Horizontal cross section (~ 2 km height) of radar reflectivity (C band) in Hurricane Isabel at ~ 1900 UTC September 12, 2003 from the lower fuselage radar on the NOAA P3 aircraft. The black arrow denotes a NOAA P3 flight segment where IWRAP data is analyzed.

16. Vertical cross section of IWRAP data at nadir in Hurricane Isabel on September 12, 2003 from 1900 – 1910 UTC along the flight segment shown by the black arrow in Fig. 15. The data shown is (a) C band reflectivity in dBZ, (b) retrieved horizontal wind

speeds in m s^{-1} and (c) retrieved vertical wind speeds in m s^{-1}. The vertical axis is exaggerated to show detail.

17. GOES infrared image of Tropical Storm Matthew (2010) on September 24 at 0645 UTC overlaid with the Global Hawk track during the NASA GRIP field experiment. The numbers on the track indicate the hour (UTC) on September 24, 2010. The blue lines overlaid on the track highlight the HIWRAP overpasses analyzed.

18. HIWRAP horizontal wind vector retrievals overlaid on Ku band reflectivity for the three Matthew overpasses highlighted in Fig. 17. The analysis grid is Lagrangian, following the NHC's estimate of the center of Matthew at the middle of each overpass with a grid spacing of 1 km. Overlaps in the three passes are averaged. The center of Matthew's circulation as defined by HIWRAP is shown by the "X" and the NHC's center estimate is shown by the "O".

19. Standard deviations in the horizontal wind speeds for the HIWRAP analysis shown in Fig. 18. The standard deviations are computed by taking the square root of the diagonal elements of $\delta \boldsymbol{g}^2$ in Eq. (10). This produces a standard deviation for each wind component so we have taken the magnitude of the horizontal standard deviations to summarize the errors in the horizontal winds.

TABLES

Table 1. Summary of HIWRAP velocity retrieval (using least squares method) errors for the Hurricane Bonnie (1998) simulated 1.8 h rotated figure-four flight pattern shown in Fig. 14. See text for details. The RMSEs are expressed in m s^{-1} and the RELs in % (rounded to the nearest whole number). The variable R is the correlation coefficient.

Exp.	Zonal			Meridional			Vertical		
Name	RMSE	REL	R	RMSE	REL	R	RMSE	REL	R
ERR1	2.09	9	0.99	2.71	10	0.99	1.72	157	0.42
ERR2	2.28	10	0.99	2.92	11	0.99	1.90	174	0.38
ERR3	2.94	13	0.99	3.64	14	0.99	2.48	227	0.29

FIGURES

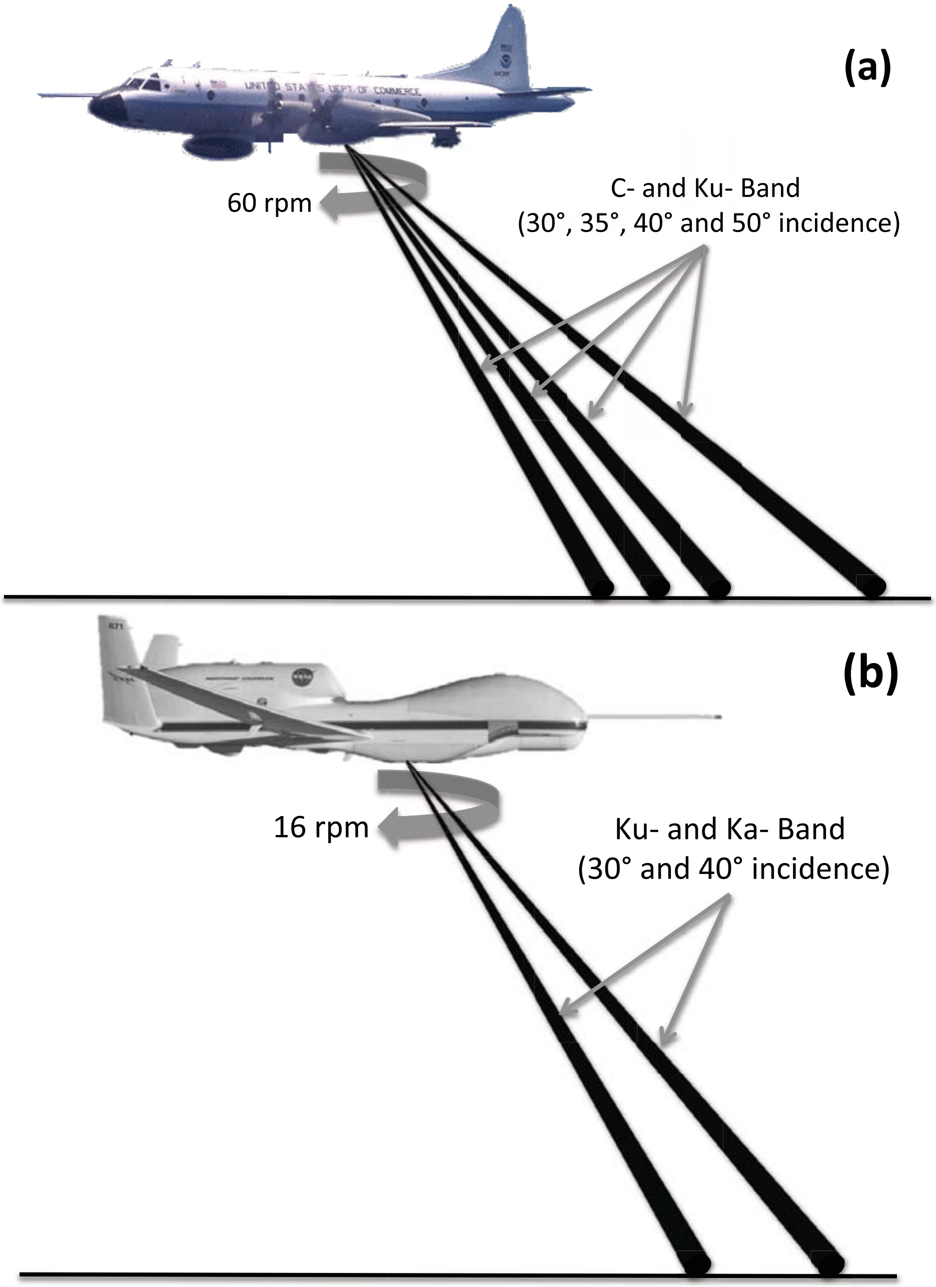

Figure 1. Measurement geometry for (a) IWRAP aboard the NOAA WP-3D aircraft with typical flight altitudes of ~ 2 – 4 km and (b) HIWRAP aboard the NASA Global Hawk aircraft with typical flight altitudes of ~ 18 – 20 km.

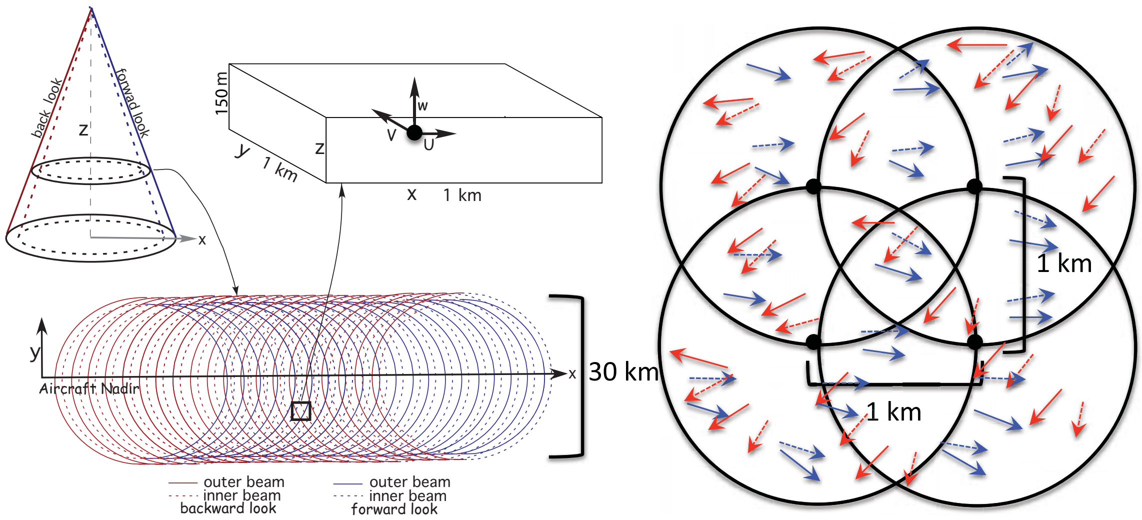

Figure 2. Scan pattern and grid structure methodology for HIWRAP. The forward and backward portions of the scan are labeled in blue and red, respectively. The inner beam (30°) and outer beam (40°) are shown in dashed and solid lines, respectively. The influence radii shown are only 1 km for illustration, but are larger for calculations. See text for more details.

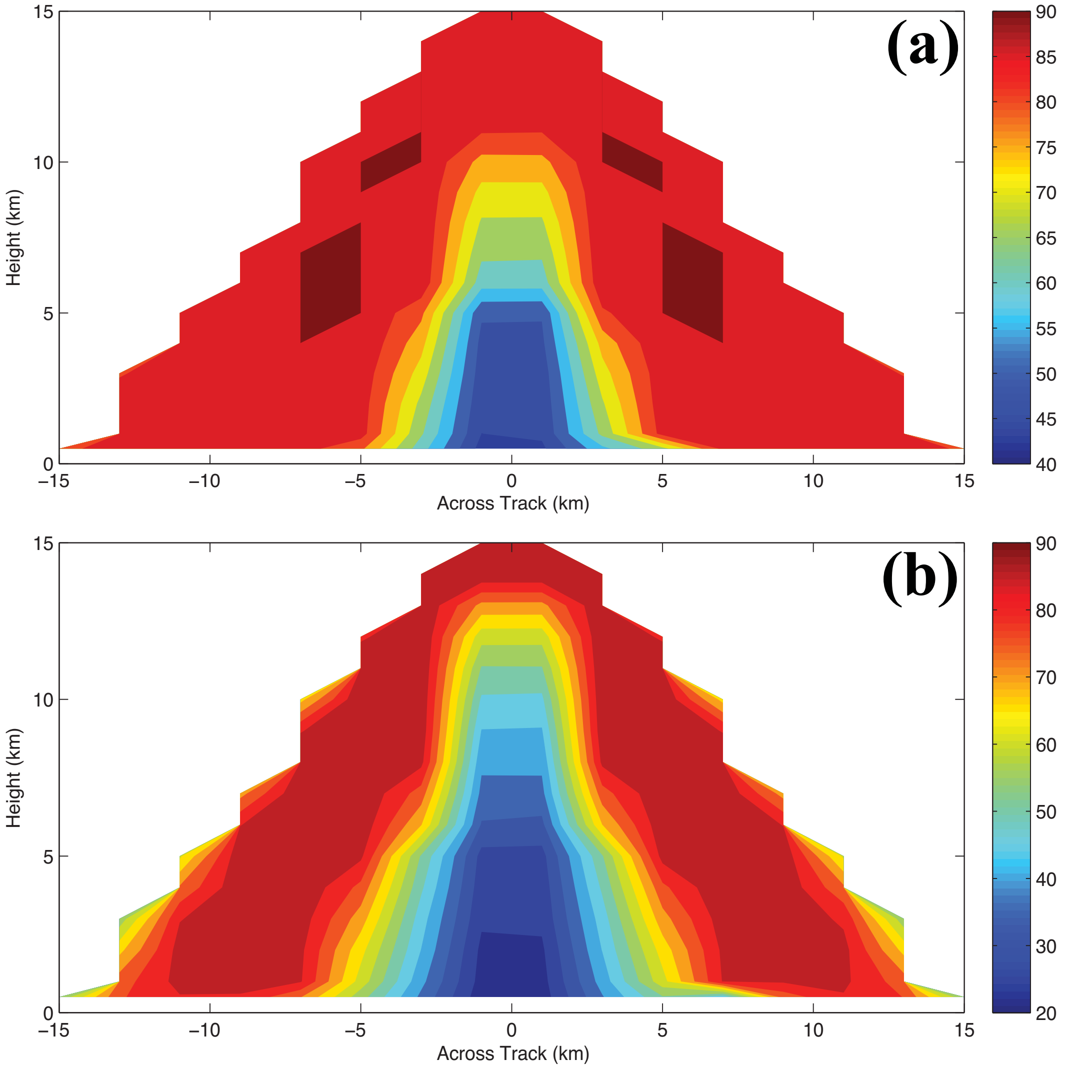

Figure 3. Maximum azimuth diversity in degrees for the HIWRAP geometry and grid structure methodology outlined in Fig. 2 only the influence radii are (a) ~ 4 km at the surface to ~ 1 km at 15 km height and (b) ~ 1.8 km at the surface to ~ 0.8 km at 15 km height. Note the color bar is different in each figure. See text for details.

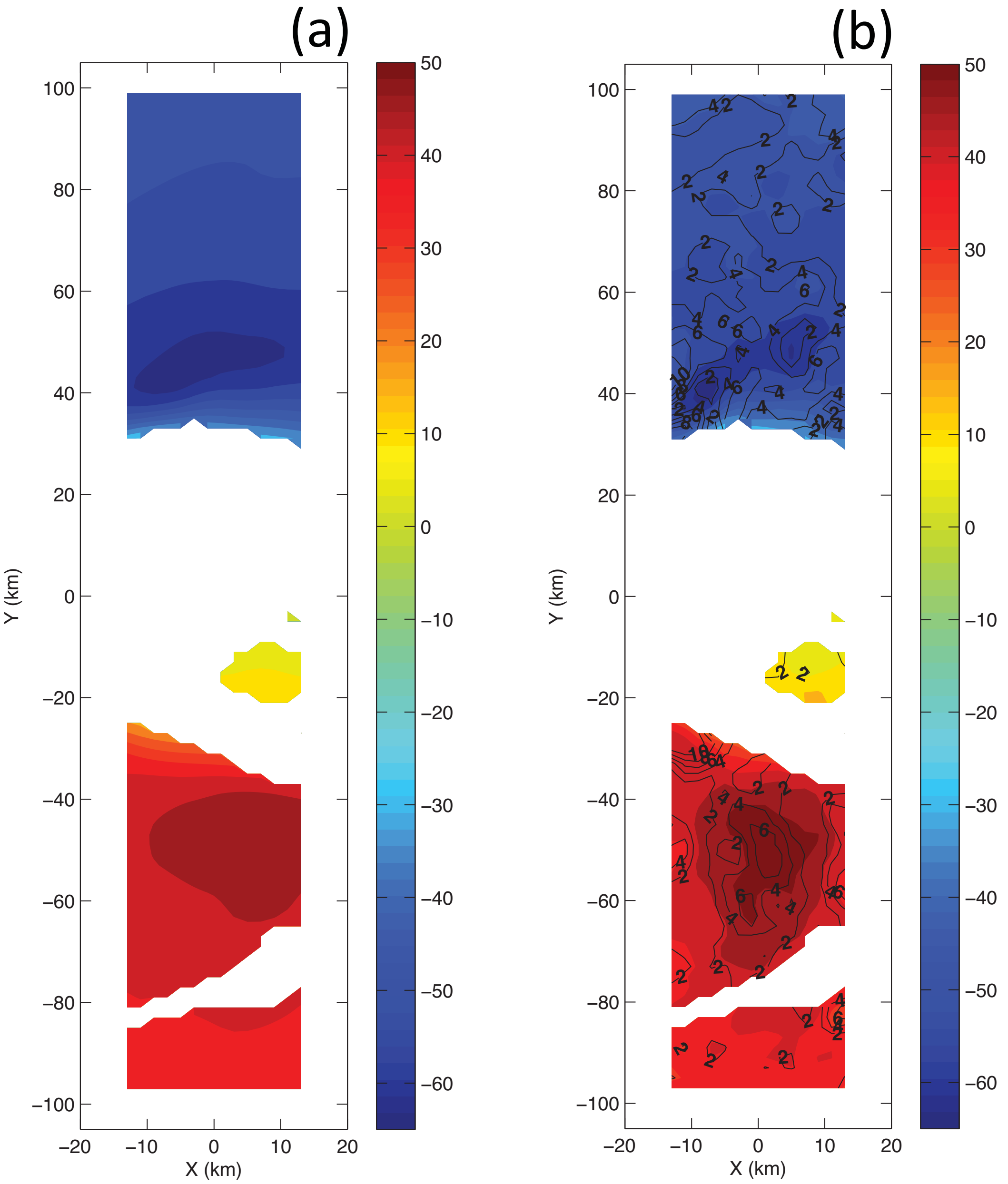

Figure 4. Simulated HIWRAP zonal (across-track) velocity at 1 km height for a northerly GH track across the eyewall of Hurricane Bonnie (1998) at 1200 UTC 23 August. The shading shows (a) the model truth field and (b) the retrieval field with the black contours revealing the RMSEs with a contour interval of 2 m s^{-1} from 2 – 10 m s^{-1}. Fields are only shown where the simulated reflectivity is greater than 0 dBZ.

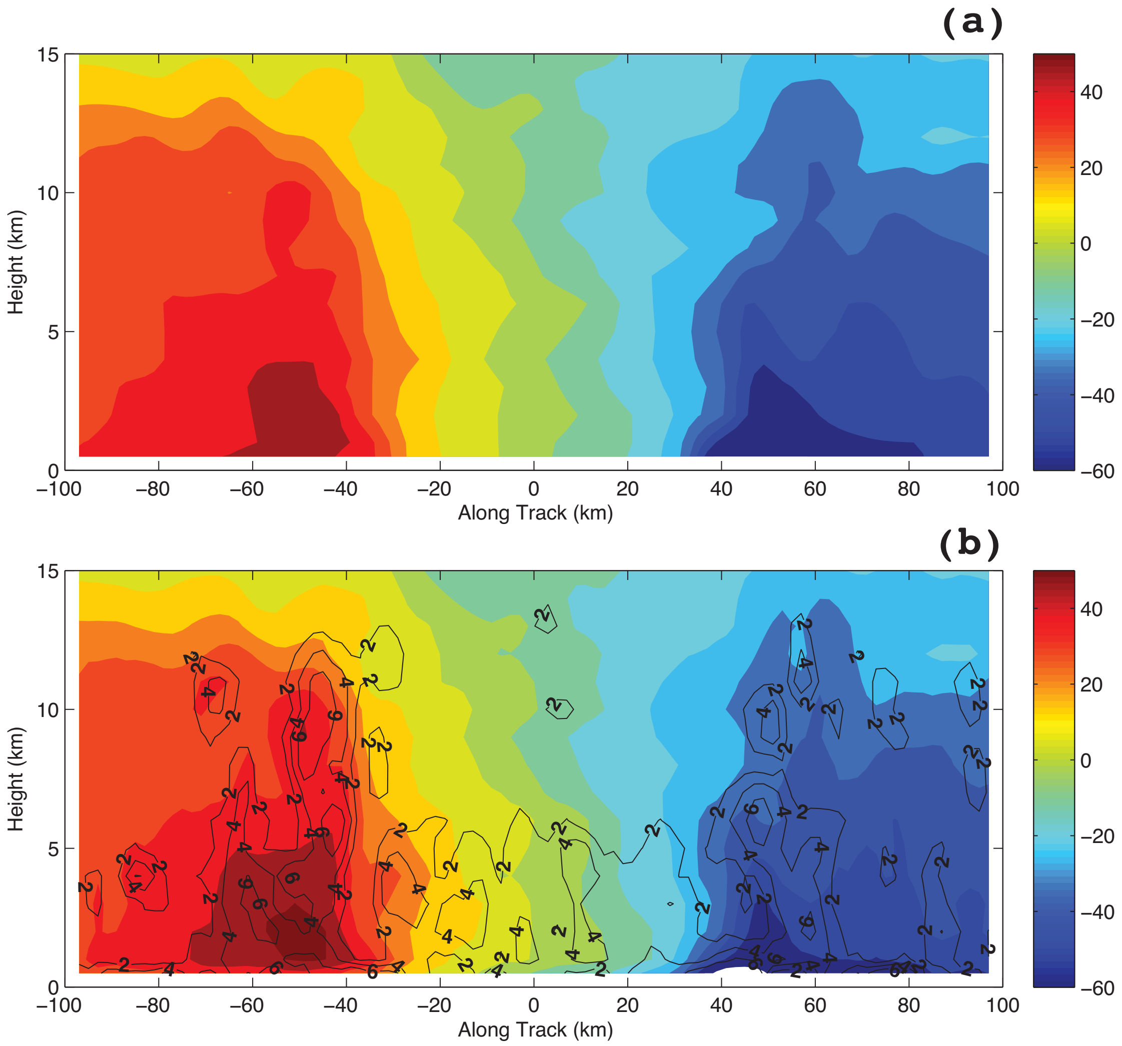

Figure 5. Comparison of (a) simulated truth and (b) retrieved zonal (across-track) velocity structure at nadir for the eyewall flight segment described in the text. The black contours in (b) show the RMSEs at 2, 4 and 6 m s^{-1}. Note that no reflectivity mask is applied to these fields and the vertical axis is exaggerated to show detail.

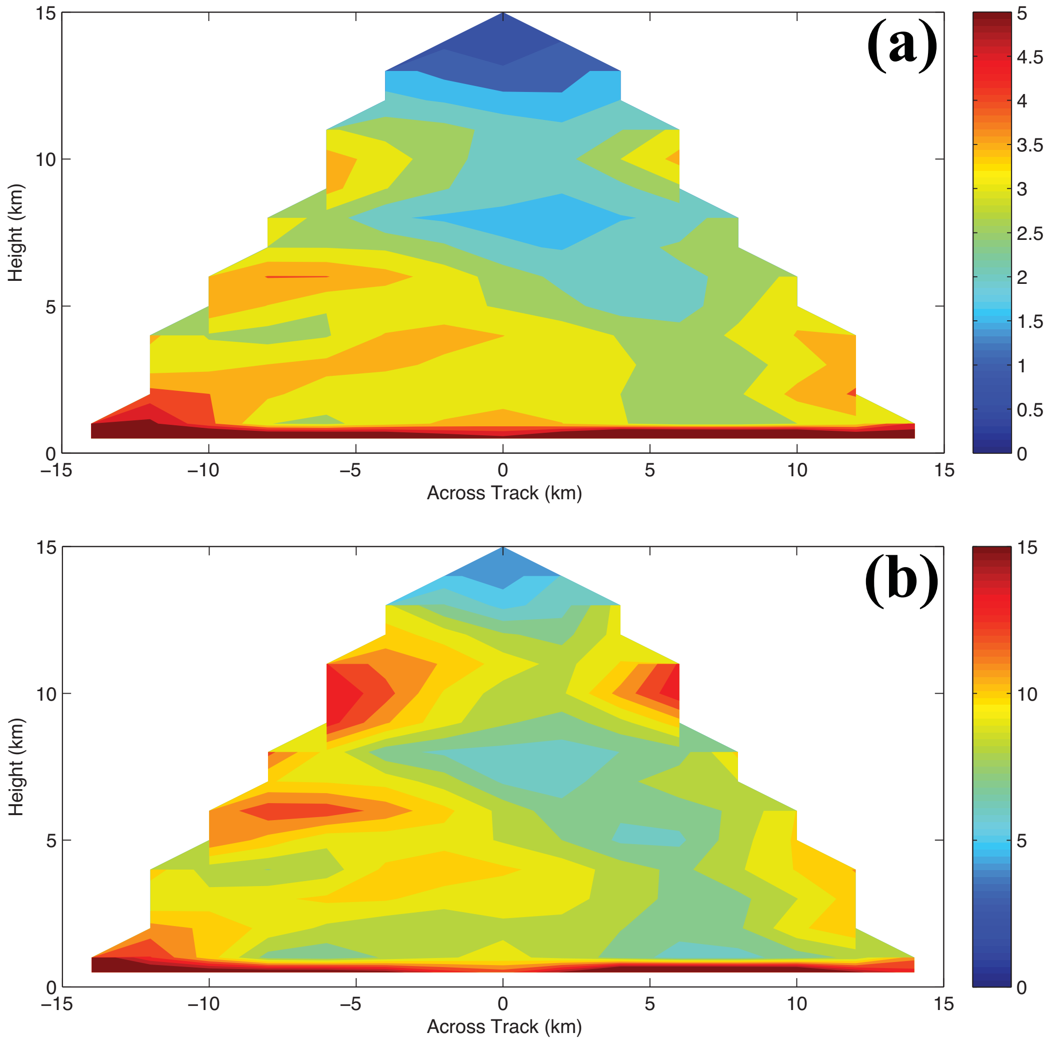

Figure 6. Simulated HIWRAP zonal (across-track) velocity retrieval errors for the same flight track as that shown in Fig 4. In these figures, the averages are taken in the along-track direction. The shading shows the (a) RMSEs and (b) RELs.

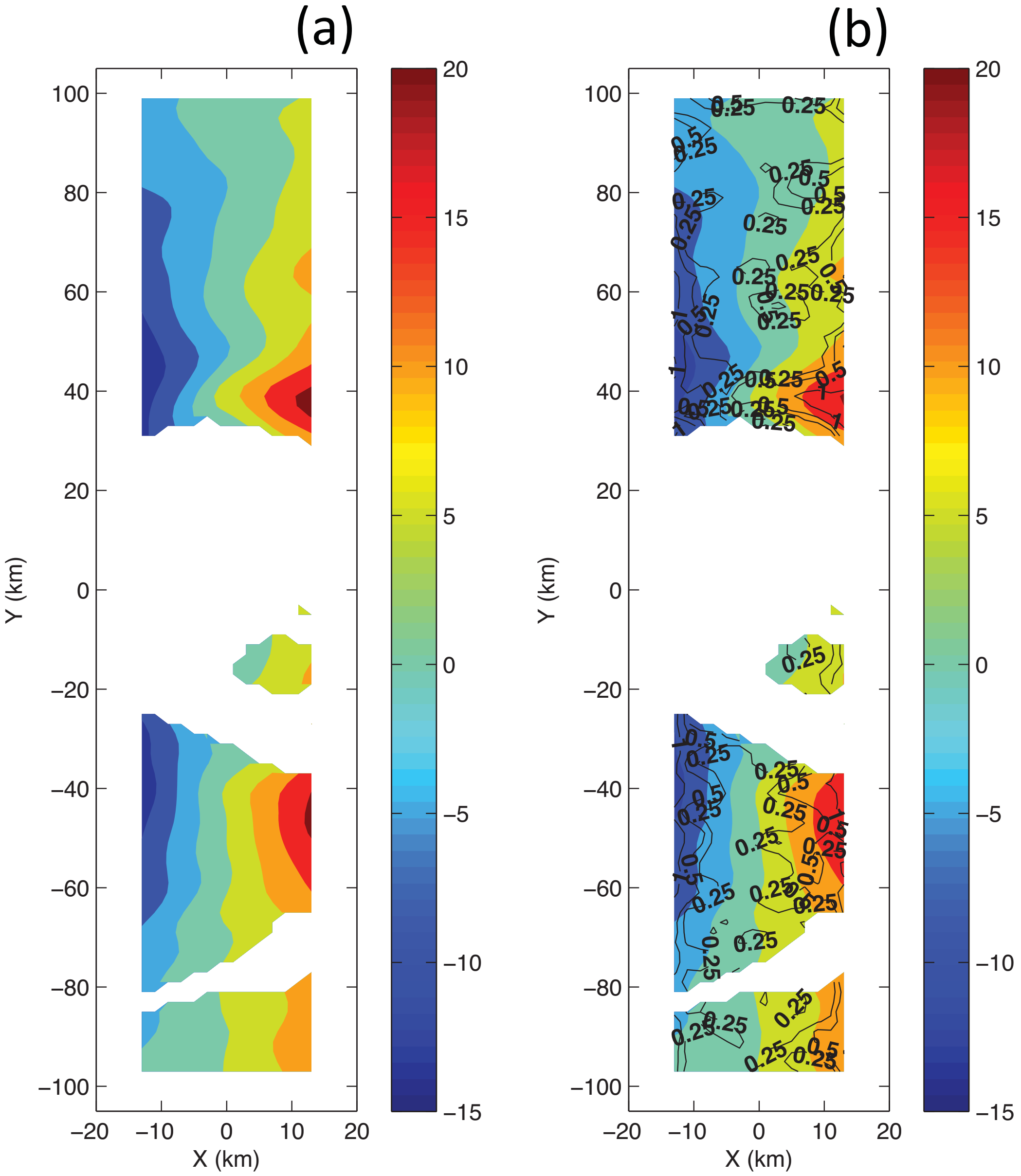

Figure 7. Same as in Fig. 4 only for the meridional (along-track) velocity with black error contours in (b) from 0.25 – 1.0 m s^{-1} with a 0.25 m s^{-1} interval.

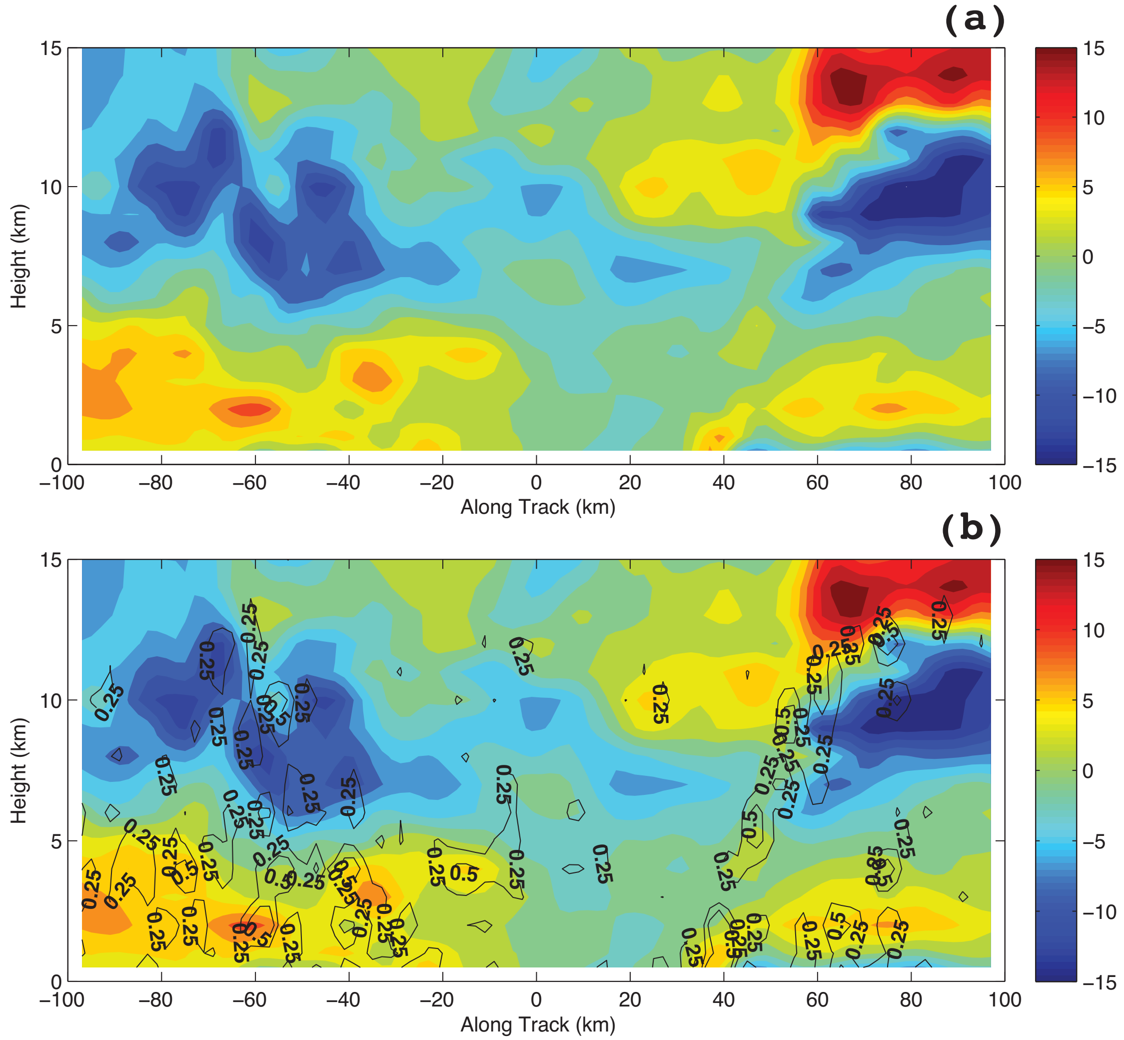

Figure 8. Same as in Fig. 5 only for the meridional (along-track) velocity. The black contours in (b) show the RMSEs at 0.25 and 0.50 m s^{-1}.

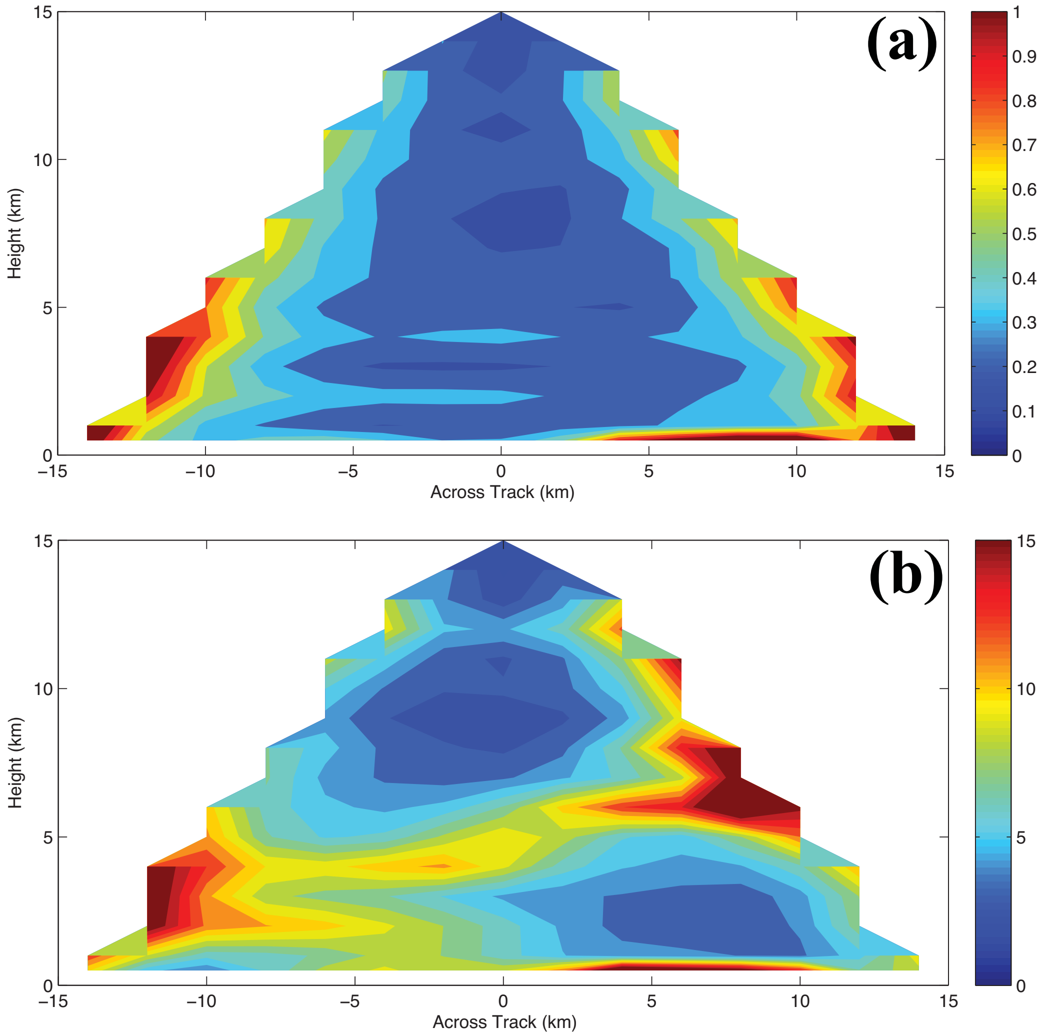

Figure 9. Same as in Fig. 6 only for the meridional (along-track) velocity.

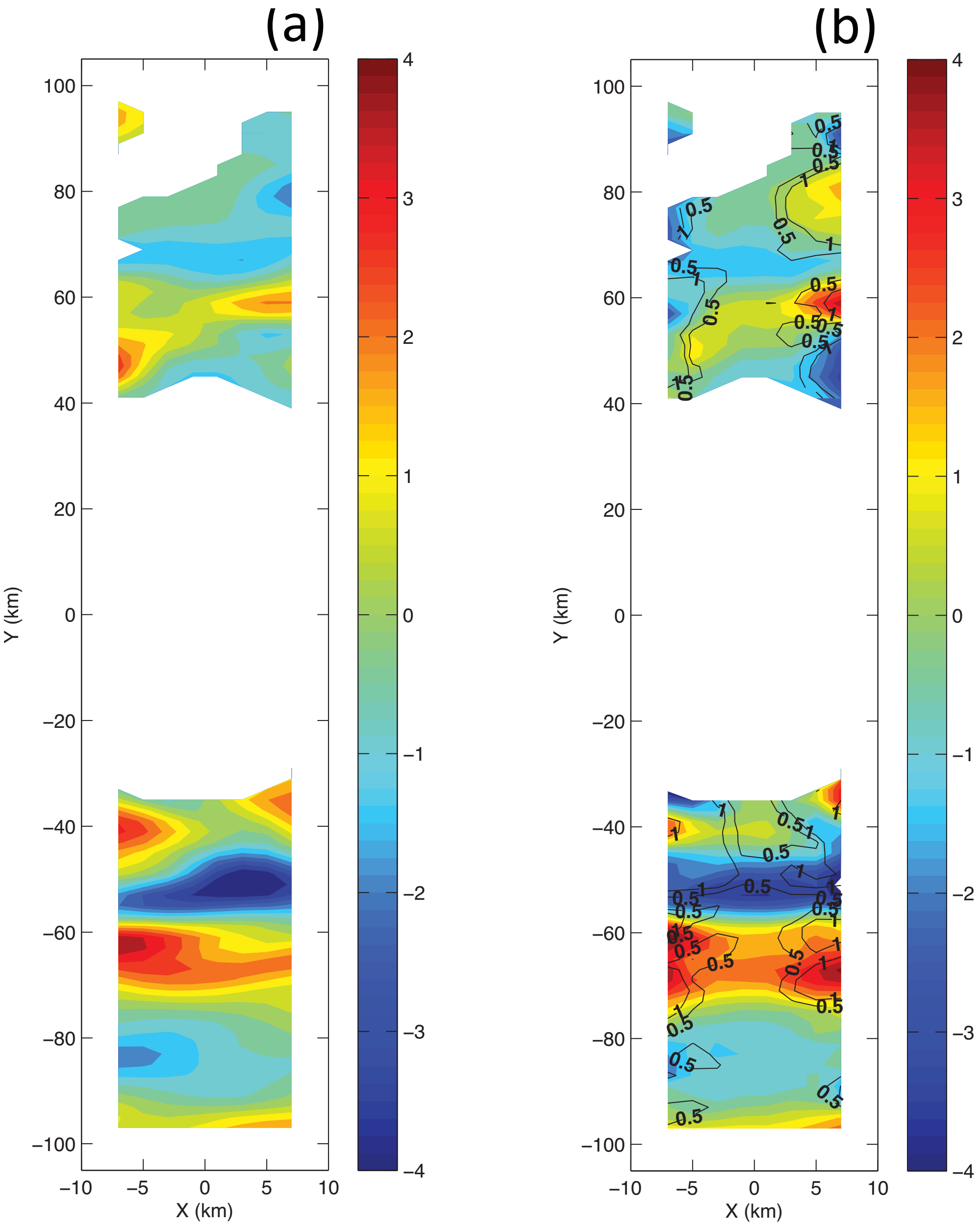

Figure 10. Same as in Fig. 4 only for the vertical velocity at 8 km height with the black error contours in (b) drawn at 0.5 and 1.0 m s^{-1}.

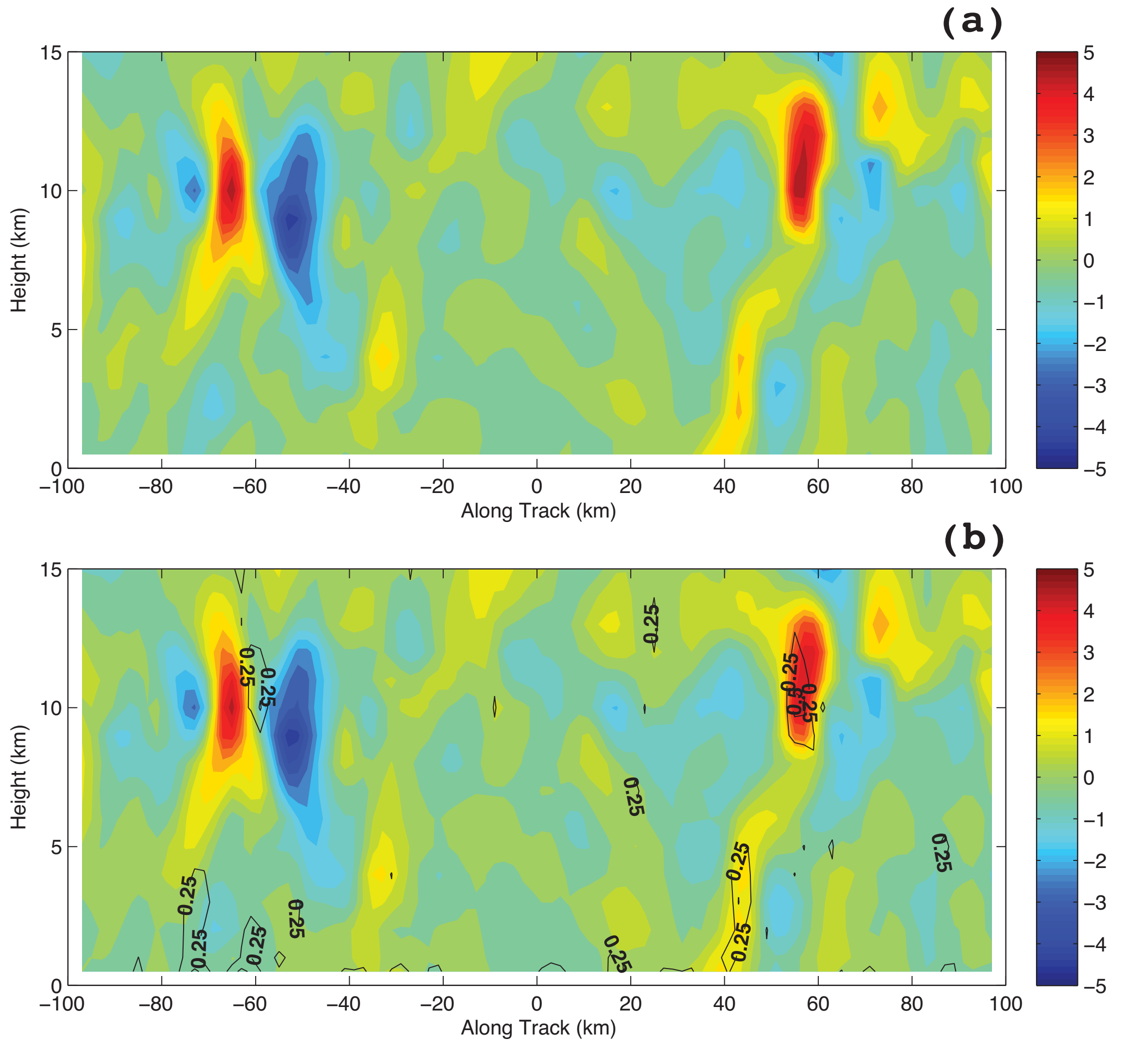

Figure 11. Same as in Fig. 5 only for the vertical velocity. The black contours in (b) show the RMSEs at 0.25 m s^{-1}.

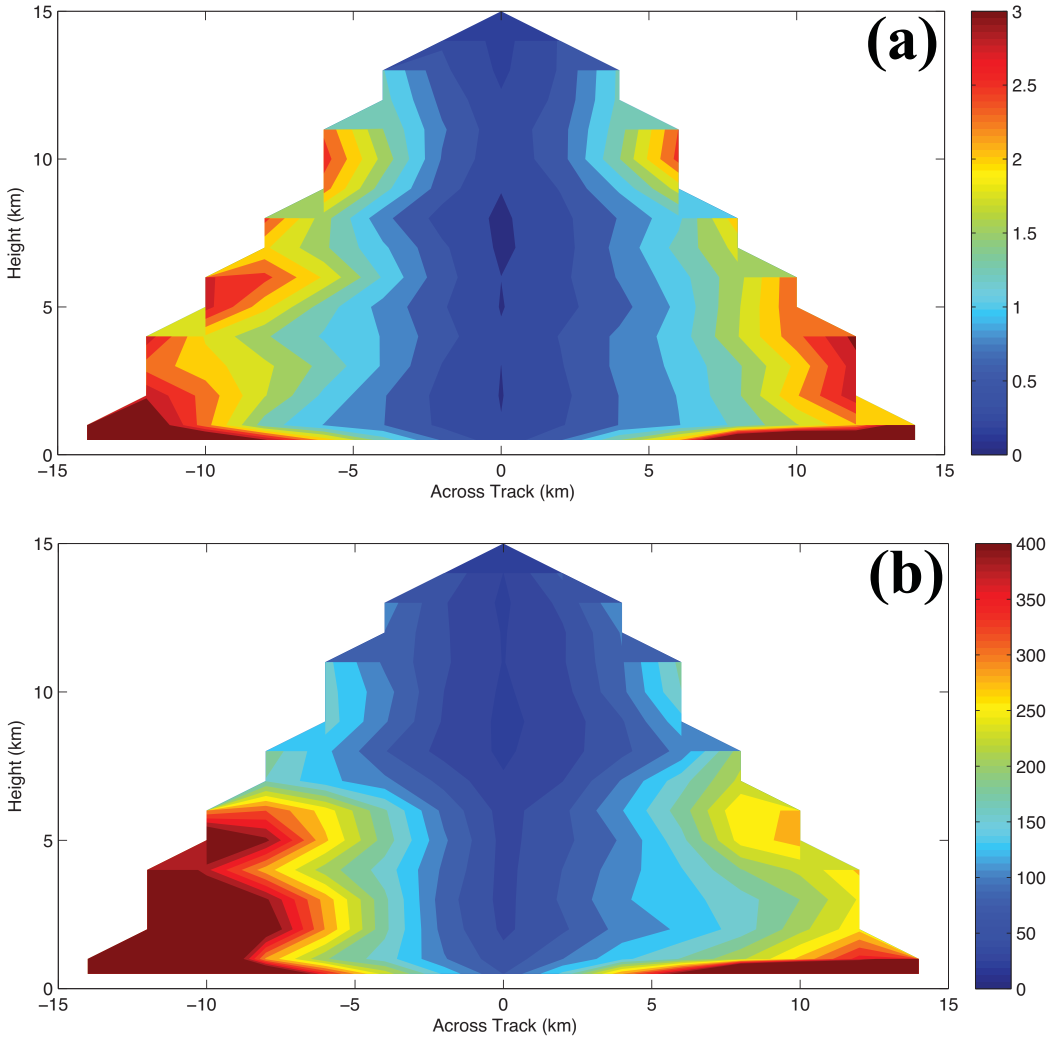

Figure 12. Same as in Fig. 6 only for the vertical velocity.

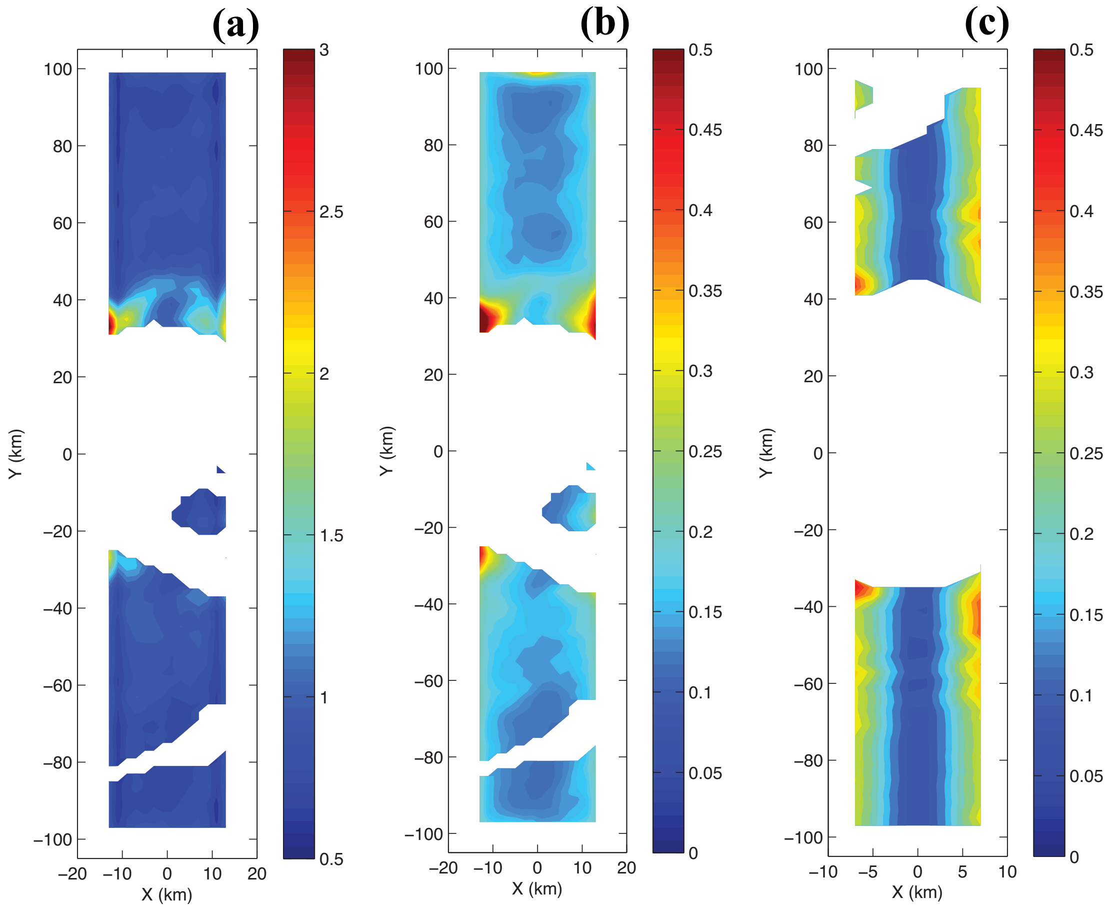

Figure 13. Standard deviations of the Cartesian wind components using an error propagation analysis with least squares theory (see text for details). The figures are (a) zonal (across-track) velocity at 1 km height (b) meridional (along-track) velocity at 1 km height and (c) vertical velocity at 8 km height. Note the different x-axis scale for the vertical velocity figure.

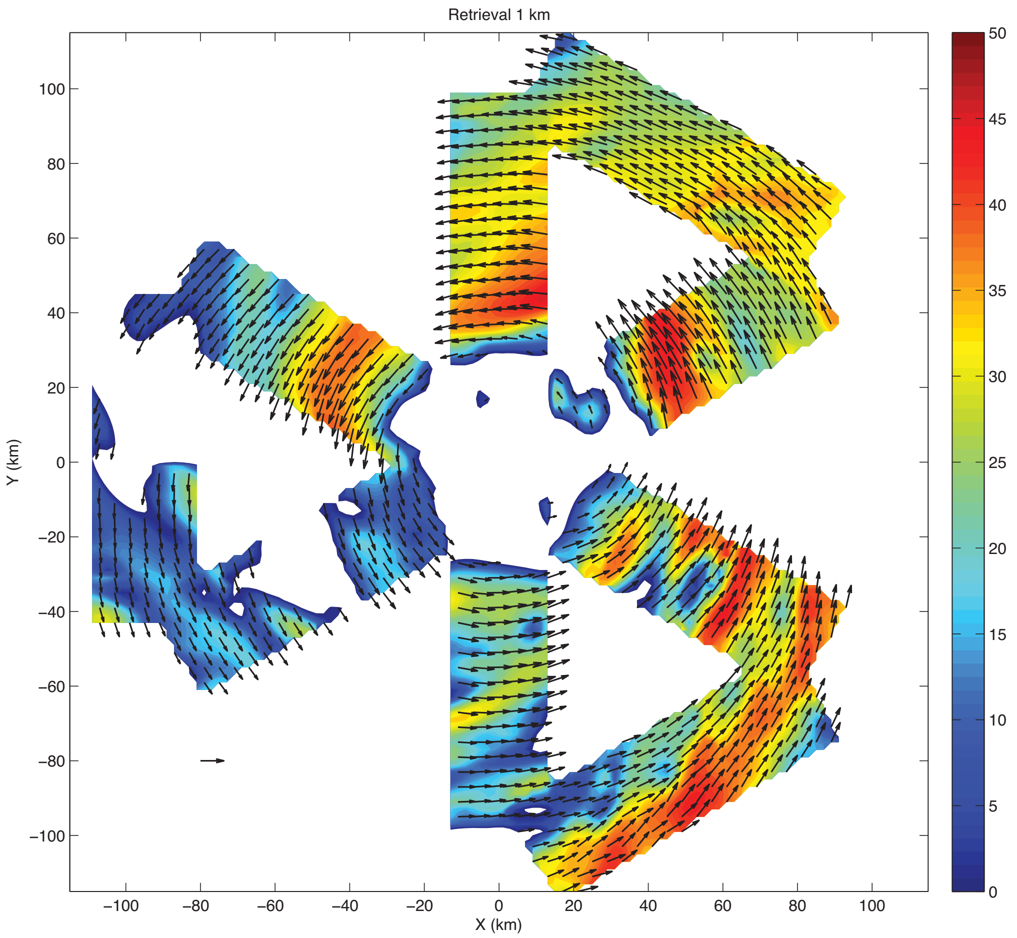

Figure 14. HIWRAP 1.8 h rotated figure-four sampling of the Bonnie numerical simulation at 1 km height starting at 1200 UTC 23 August 1998. In this figure, the winds are from the least squares retrieval method. The shading is simulated reflectivity in dBZ and the reference arrow at (-80, -80) is 50 m s^{-1}. The large hole (no reflectivity/winds) in the center is the large eye of the simulated Bonnie.

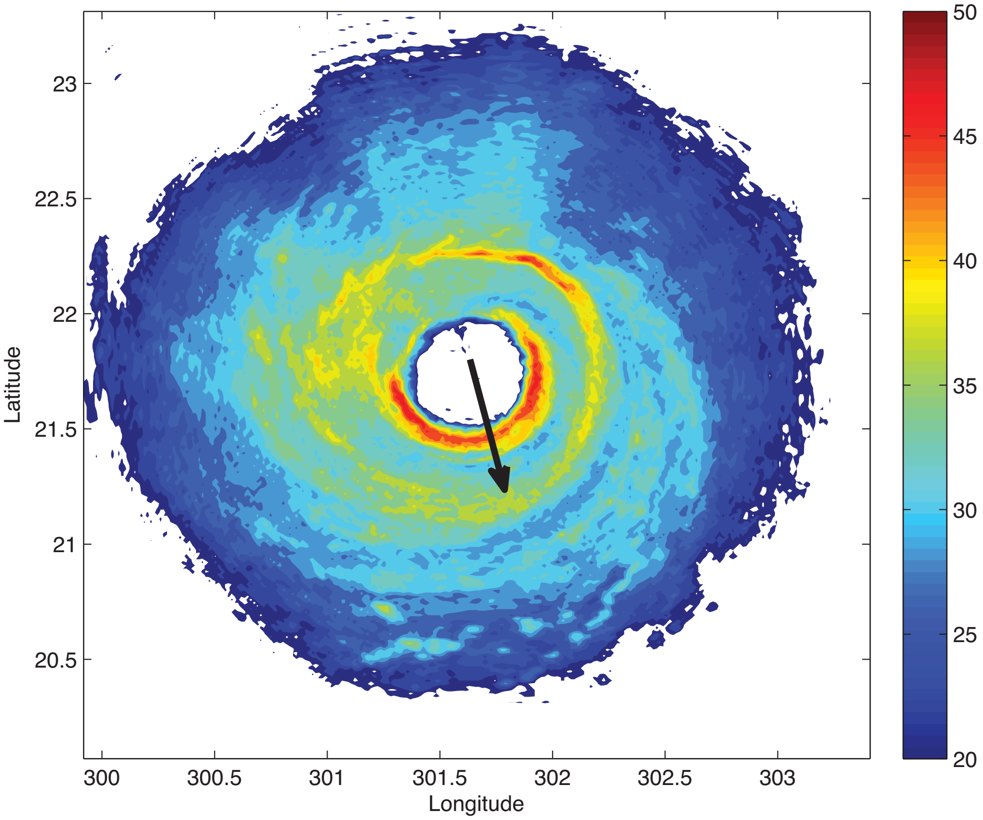

Figure 15. Horizontal cross section (~ 2 km height) of radar reflectivity (C band) in Hurricane Isabel at ~ 1900 UTC September 12, 2003 from the lower fuselage radar on the NOAA P3 aircraft. The black arrow denotes a NOAA P3 flight segment where IWRAP data is analyzed.

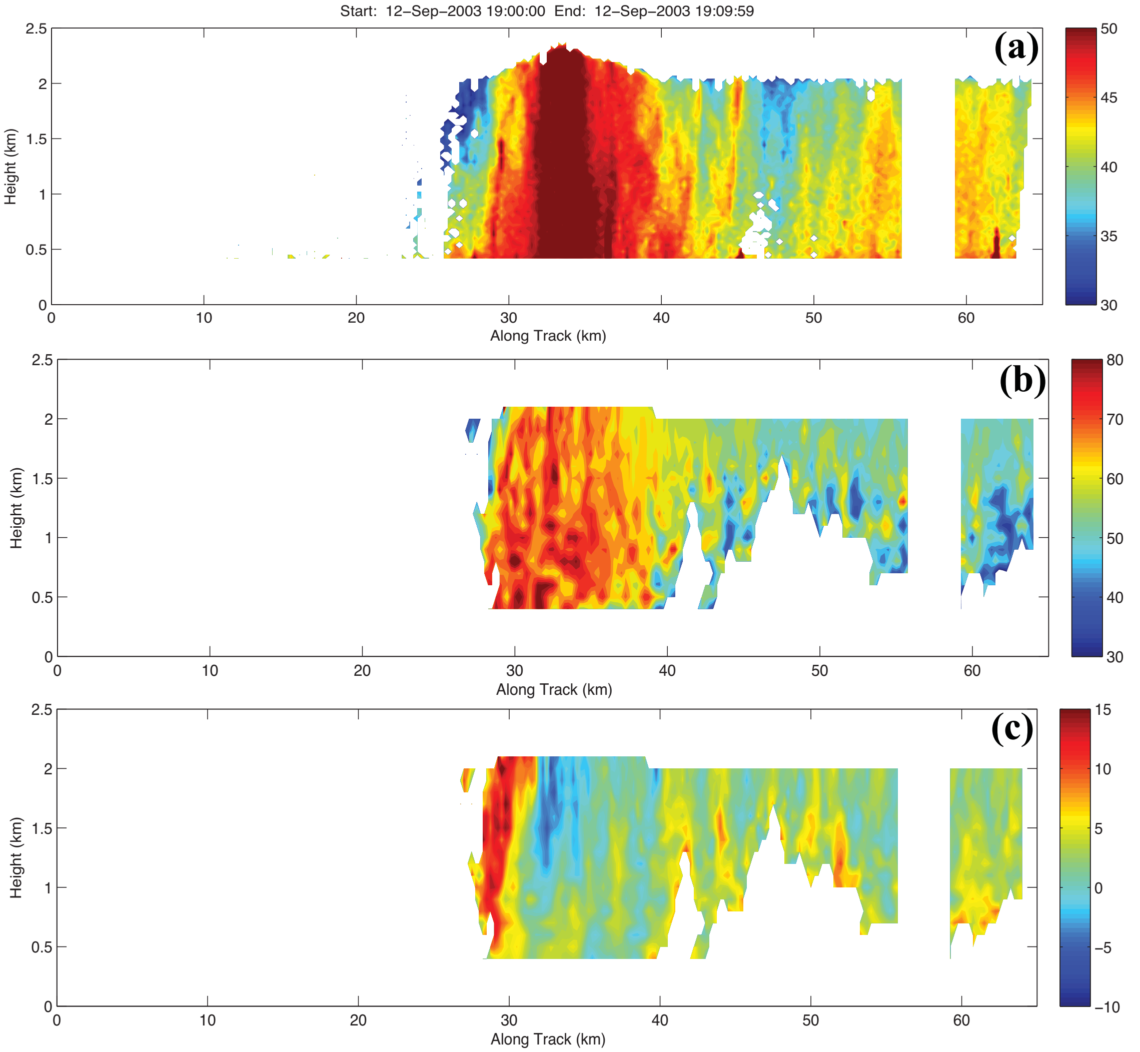

Figure 16. Vertical cross section of IWRAP data at nadir in Hurricane Isabel on September 12, 2003 from 1900 – 1910 UTC along the flight segment shown by the black arrow in Fig. 15. The data shown is (a) C band reflectivity in dBZ, (b) retrieved horizontal wind speeds in m s^{-1} and (c) retrieved vertical wind speeds in m s^{-1}. The vertical axis is exaggerated to show detail.

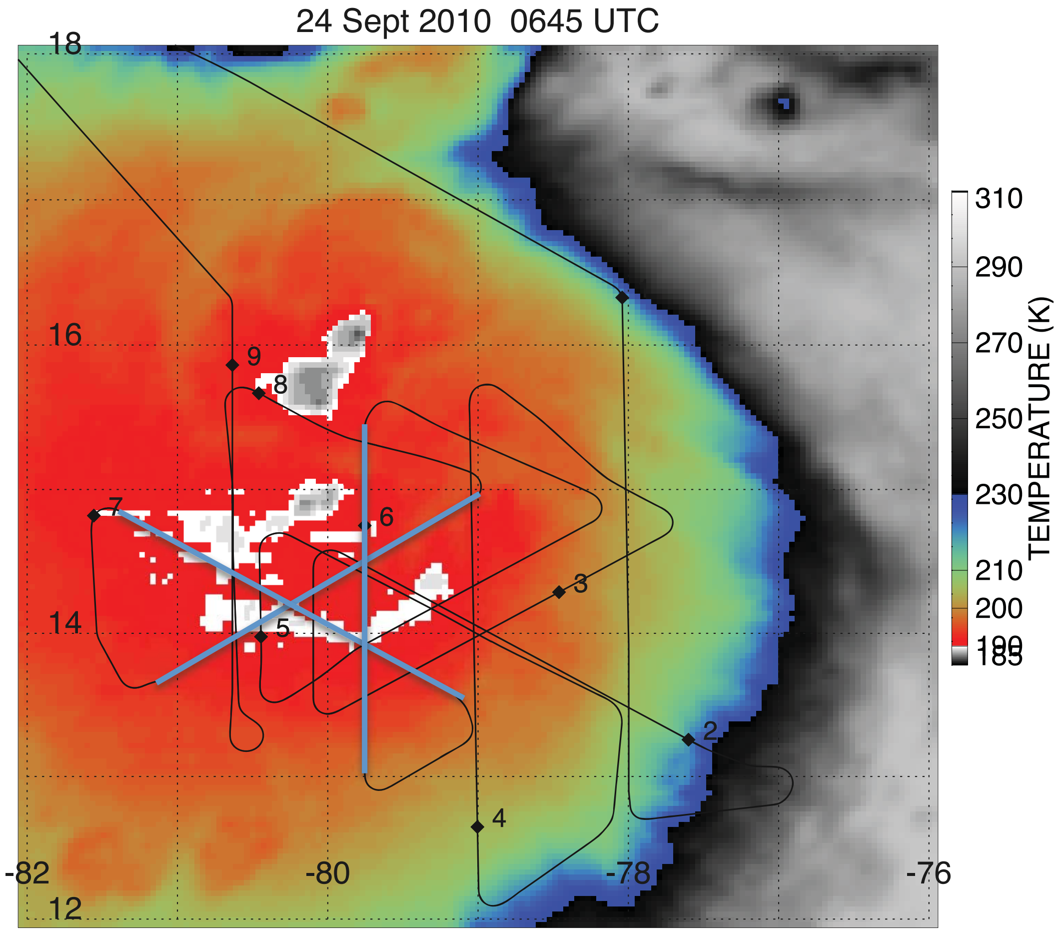

Figure 17. GOES infrared image of Tropical Storm Matthew (2010) on September 24 at 0645 UTC overlaid with the Global Hawk track during the NASA GRIP field experiment. The numbers on the track indicate the hour (UTC) on September 24, 2010. The blue lines overlaid on the track highlight the HIWRAP overpasses analyzed.

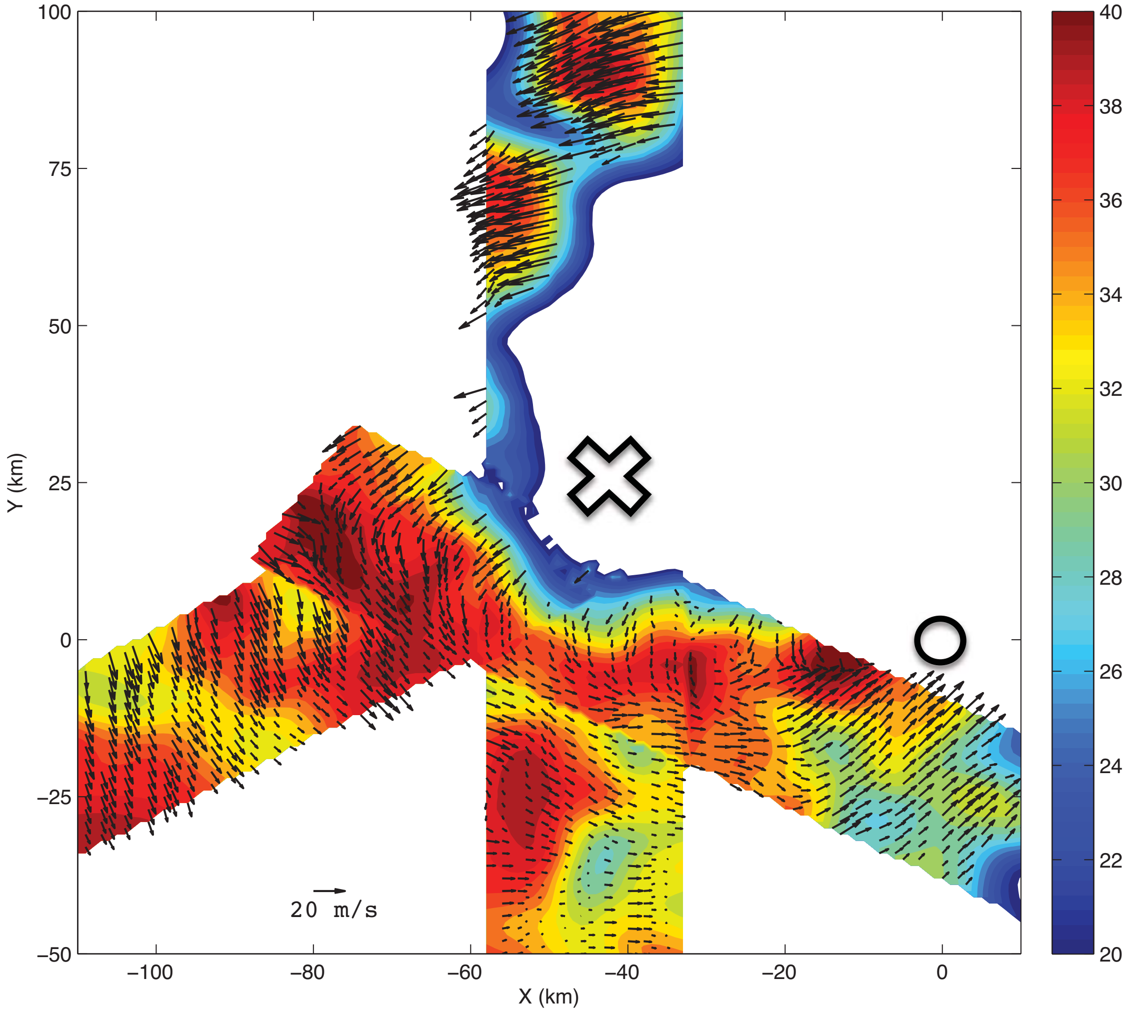

Figure 18. HIWRAP horizontal wind vector retrievals overlaid on Ku band reflectivity for the three Matthew overpasses highlighted in Fig. 17. The analysis grid is Lagrangian, following the NHC's estimate of the center of Matthew at the middle of each overpass with a grid spacing of 1 km. Overlaps in the three passes are averaged. The center of Matthew's circulation as defined by HIWRAP is shown by the "X" and the NHC's center estimate is shown by the "O".

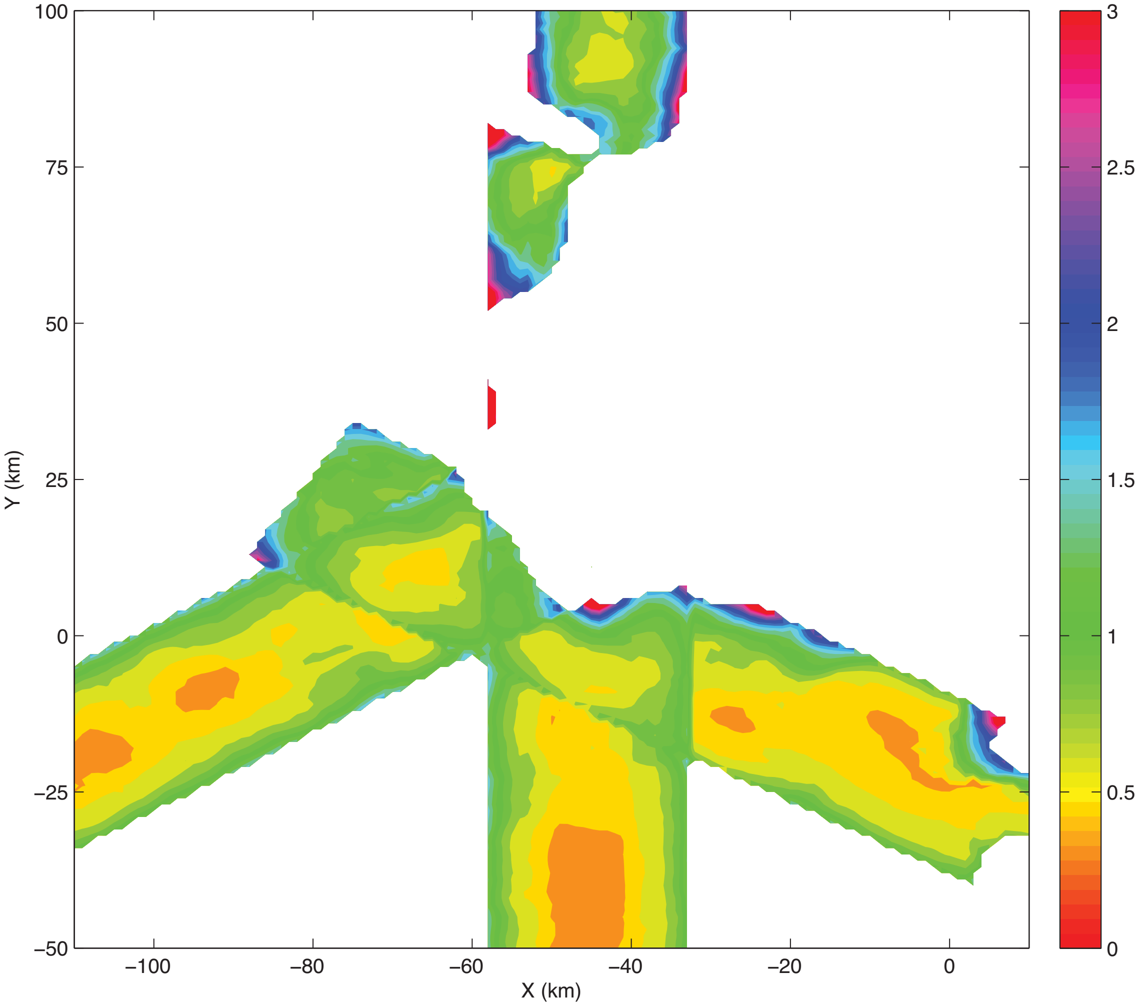

Figure 19. Standard deviations in the horizontal wind speeds for the HIWRAP analysis shown in Fig. 18. The standard deviations are computed by taking the square root of the diagonal elements of $\delta \boldsymbol{g}^2$ in Eq. (10). This produces a standard deviation for each wind component so we have taken the magnitude of the horizontal standard deviations to summarize the errors in the horizontal winds.